



3 4456 0375526 5

ORNL/TM-12327

ORNL

OAK RIDGE  
NATIONAL  
LABORATORY

MARTIN MARIETTA

Conical Geometry for Sagittal  
Focusing as Applied to X Rays  
from Synchrotrons

G. E. Ice  
C. J. Sparks

OAK RIDGE NATIONAL LABORATORY  
CENTRAL RESEARCH LIBRARY  
CIRCULATION SECTION  
4500N ROOM 175  
**LIBRARY LOAN COPY**  
DO NOT TRANSFER TO ANOTHER PERSON  
If you wish someone else to see this  
report, send in name with report and  
the library will arrange a loan.  
UCRL 7269 (REV. 5/75)

MANAGED BY  
MARTIN MARIETTA ENERGY SYSTEMS, INC.  
FOR THE UNITED STATES  
DEPARTMENT OF ENERGY

This report has been reproduced directly from the best available copy.

Available to DOE and DOE contractors from the Office of Scientific and Technical Information, P.O. Box 62, Oak Ridge, TN 37831; prices available from (615) 576-8401, FTS 626-8401.

Available to the public from the National Technical Information Service, U.S. Department of Commerce, 5285 Port Royal Rd., Springfield, VA 22161.

This report was prepared as an account of work sponsored by an agency of the United States Government. Neither the United States Government nor any agency thereof, nor any of their employees, makes any warranty, express or implied, or assumes any legal liability or responsibility for the accuracy, completeness, or usefulness of any information, apparatus, product, or process disclosed, or represents that its use would not infringe privately owned rights. Reference herein to any specific commercial product, process, or service by trade name, trademark, manufacturer, or otherwise, does not necessarily constitute or imply its endorsement, recommendation, or favoring by the United States Government or any agency thereof. The views and opinions of authors expressed herein do not necessarily state or reflect those of the United States Government or any agency thereof.

504  
25

Metals and Ceramics Division

**CONICAL GEOMETRY FOR SAGITTAL FOCUSING AS  
APPLIED TO X RAYS FROM SYNCHROTRONS**

G. E. Ice  
C. J. Sparks

Date Published-June 1993

NOTICE: This document contains information of  
a preliminary nature. It is subject  
to revision or correction and therefore  
does not represent a final report.

Prepared for  
DOE Office of Basic Energy Sciences  
KC 02 02 02 0

Prepared by the  
OAK RIDGE NATIONAL LABORATORY  
Oak Ridge, Tennessee 37831-6285  
managed by  
MARTIN MARIETTA ENERGY SYSTEMS, INC.  
for the  
U.S. DEPARTMENT OF ENERGY  
under contract DE-AC05-84OR21400





## TABLE OF CONTENTS

	<u>Page</u>
LIST OF FIGURES .....	v
ABSTRACT .....	1
1. INTRODUCTION .....	1
2. CRYSTAL VERSUS MIRROR FOCUSING .....	5
3. CONICAL CRYSTAL GEOMETRY .....	8
4. RAY-TRACING RESULTS .....	13
5. ALIGNMENT AND OPERATION .....	17
5.1 BENDING MECHANISM .....	17
5.2 STIFFENING AGAINST ANTICLASTIC BENDING .....	20
5.3 ALIGNMENT OF MONOCHROMATOR .....	22
5.4 BENDING ERRORS .....	25
5.4.1 Focus .....	25
5.4.2 Twist .....	25
5.4.3 Cone Angle .....	27
5.4.4 Even (Symmetric) Bending Moment .....	27
5.5 PERFORMANCE AND FUTURE APPLICATIONS .....	27
6. CONCLUSION .....	28
7. ACKNOWLEDGMENTS .....	29
8. REFERENCES .....	29



## LIST OF FIGURES

<u>Figure</u>	<u>Page</u>
<p>1 (a) Diagram of nondispersive X-ray optics with a source divergence <math>\delta</math> in the scattering (meridional) plane. The central ray diffracts with Bragg angle <math>\theta</math> on both parallel crystals. A ray with meridional divergence <math>\delta</math> from the central ray diffracts with angle <math>\theta + \delta</math> on both crystals. The energy diffracted along the two ray paths differs according to Bragg's law.</p> <p>(b) A nondispersive arrangement with one crystal bent for meridional focusing. With the first crystal bent to the Johann or Johansson geometry for focusing, only the central ray makes the same Bragg angle on both crystals. The magnitude of the angular difference between the Bragg angles on the first and second crystal depends on the divergence from the central ray, <math>\delta</math>, and the radius of curvature . . . . .</p>	4
<p>2 (a) Geometry of doubly focusing X-ray optic: <math>F_1</math> source to optics distance, <math>F_2</math> optic to image distance, <math>R_s</math> the sagittal curvature, and <math>R_m</math> the meridional curvature. The central ray is reflected with an angle <math>\theta</math>. (b) Top view showing sagittal focusing with the characteristic smile of the beam intercept on the curved surface. (c) Side view of sagittal focusing shows how sagittal focusing must mix the sagittal divergence into the meridional divergence to maintain a good focal spot. (d) In-plane or meridional focusing with meridional curvature <math>R_m</math>. Since <math>R_m = R_s/\sin^2\theta</math>, the curvature required for in-plane focusing is much less than for sagittal focusing, especially at glancing angles . . . . .</p>	6
<p>3 (a) Geometry for the conical or cylindrical-crystal flat-crystal nondispersive monochromator. In the meridional (scattering) plane, the bent crystal acts as a flat crystal to the first flat crystal in the nondispersive geometry. (b) Geometry for determining the angle <math>\theta_c</math> of a ray with horizontal divergence <math>\psi</math> striking a conical surface . . . . .</p>	9
<p>4 The cone angle <math>\Delta</math> as a function of magnification <math>M</math>. At <math>M = 0.33</math>, the cone angle goes from negative to positive. Also plotted are the sagittal focusing radii, <math>N = R_s = 2MF_1\sin\theta/(1+M)</math>, as a function of <math>M</math> for <math>F_1 = 20</math> m and for <math>F_1 + F_2 = 40</math> m. Note that the radii are multiplied by a factor of 10 to put them on the same scale as the cone angle <math>\Delta</math> . . . . .</p>	12
<p>5 Modeled optical geometry used in the ray-tracing calculations of the conical crystal focusing. The in-plane (meridional) focusing mirror is used to focus the small vertical synchrotron radiation divergence. The sagittal focusing crystal is used to collect and focus 15 mrad of synchrotron radiation divergence. Ray-tracing programs are particularly useful for studying the effect of source size on focusing performance . . . . .</p>	14

<u>Figure</u>	<u>Page</u>
6 RMS image size for a 10 or 30 keV (1.6 or 4.8 fJ) x-rays from a point source with 6 mrad horizontal divergence focused by a conical crystal ( $F_1 = 30$ m). Both horizontal and vertical RMS image sizes are plotted as a function of magnification . . . . .	14
7 Comparison of the transmission through a 200- $\mu$ m-diam pinhole with $M = 0.33$ and $M = 1$ . For this comparison, the source size and vertical divergence are modeled after the anticipated parameters for a wiggler line at the APS (see text). The comparison is virtually identical for an APS bending magnet line . . . . .	15
8 Performance of the model focusing system of Fig. 5 for $F_1 = 10$ m, $M = 1$ , and $2\psi = 15$ mrad. The crystals were assumed to be $\text{Si}_{111}$ . The source was assumed to have an RMS horizontal and vertical size of 0.4 by 0.05 $\text{mm}^2$ . Decreased transmission at higher energies results from the inability of the focusing crystal monochromator to accept the full horizontal source size . . . . .	16
9 Illustration of the four-rod-bending scheme and a ribbed crystal to suppress anticlasic bending. Two rods are fixed to an optically polished plate while the ends of the other two rods are independently controlled by stepping motors with submicron resolution. Designs where either the inside or outside rods are moved have been successfully tested . . . . .	18
10 Four-point-bending schematic for a uniform beam showing forces $W_1$ and $W_2$ applied at the outer points. The beam is bent by a displacement $F_1$ from the relaxed beam at the end with force $W_1$ and by $F_2$ from the relaxed beam at the end with force $W_2$ . The maximum central deflection is $F_C$ . Below the four-point-bending schematic is the bending moment diagram. When $W_1 = W_2$ , the displacements $F_1 = F_2$ and the central portion of the beam experience a constant pure bending moment (no shear forces) . . . . .	19
11 An unsupported plate bent to a sagittal radius $R_S$ develops an anticlasic curvature $R_A$ , which is larger than $R_S$ by the inverse of Poisson's ratio, $\sigma$ , and produces an error $\Delta\theta E$ in scattering angle . . . . .	20
12 (a) The alignment controls needed for the two-crystal monochromator include vertical displacement and $\chi$ , $\theta$ , and $\phi$ rotation axes. The two crystals can have a parallelism error in their chi tilt $\Delta\chi$ . The crystal can also be rotated by $\phi$ . (b) Unfocused and focused image when the scattering plane of the monochromator is not perpendicular to the plane of the storage ring. (c) Diagram showing how a misalignment of the horizontal translation axis for the linear slide results in a change in the crystal-crystal spacing, $h$ , producing a vertical displacement of the beam as energy is scanned . . . . .	24

- 13 (a-e) Schematic showing how four orthogonal bending motions are used to achieve a conical curvature for a four-line loaded plate. (a-b) If all four ends of the bender illustrated in Fig. 7 are driven equally, the average radius is changed. (c) If diagonally opposing motors are driven in the same direction, then the plate is twisted. (d) When front and back ends are driven, then the cone angle  $\Delta$  is changed. (e) Left-side motors driven in the opposite direction of right-side motors cause the radius to increase on one side of the crystal and decrease on the other side . . . . . 26



# CONICAL GEOMETRY FOR SAGITTAL FOCUSING AS APPLIED TO X RAYS FROM SYNCHROTRONS\*

G. E. Ice and C. J. Sparks

## ABSTRACT

We describe a method for simultaneously focusing and monochromatization of X rays from a fan of radiation having up to 15 mrad divergence in one dimension. This geometry is well suited to synchrotron radiation sources at magnifications of one-fifth to two and is efficient for X-ray energies between 3 and 40 keV (0.48 and 6.4 fJ). The method uses crystals bent to part of a cone for sagittal focusing and allows for the collection of a larger divergence with less mixing of the horizontal into the vertical divergence than is possible with X-ray mirrors. We describe the geometry required to achieve the highest efficiency when a conical crystal follows a flat crystal in a nondispersive two-crystal monochromator. At a magnification of one-third, the geometry is identical to a cylindrical focusing design described previously. A simple theoretical calculation is shown to agree well with ray-tracing results. Minimum aberrations are observed at magnifications near one. Applications of the conical focusing geometry to existing and future synchrotron radiation facilities are discussed.

---

## 1. INTRODUCTION

Crystals are used to focus X-ray beams with large divergences.<sup>1-3</sup> Compared to total external reflection mirrors, the scattering angles from crystals are larger which allows crystals to collect larger divergences with smaller aberrations. The recent development of high-brilliance (photons/sec/eV/mrad<sup>2</sup>/mm<sup>2</sup>) synchrotron sources has created the need for X-ray optics that can monochromatize and focus over a wide energy range.<sup>4,5</sup> Particularly critical is the need for focusing X rays with energies above 10 keV (1.6 fJ). There are several

---

\*Research performed in part at the Oak Ridge National Laboratory Beamline X-14 at the National Synchrotron Light Source, Brookhaven National Laboratory, sponsored by the Division of Materials Sciences and Division of Chemical Sciences, U.S. Department of Energy, under contract DE-AC05-84OR21400 with Martin Marietta Energy Systems, Inc.

standard X-ray focusing schemes: separate function designs with mirror focusing and a separate monochromator,<sup>6</sup> meridional focusing using Johann<sup>1</sup> or Johannson crystal optics,<sup>2,7,8</sup> and sagittal focusing mosaic crystal optics.<sup>9</sup> Each of these systems has limitations either in angular acceptance, range of energy tunability, or ability to preserve beam brilliance.

Recently, a new class of energy-tunable focusing monochromators has been developed: the sagittal-focusing, dynamically bent crystal monochromators.<sup>10-13</sup> These monochromators are similar to the Von Hámos X-ray spectrometer<sup>3</sup> but are optimized to condense the monochromatic fan of X rays produced by the reflection of synchrotron radiation from a flat crystal. At magnifications ( $M$ ) near one-third, a simple, cylindrically curved crystal was shown to intercept a fan of radiation at a constant Bragg angle.<sup>10</sup> The cylindrical geometry allowed the construction of a simple, nondispersive monochromator with focusing and wide-energy tunability.<sup>10-13</sup>

Here we discuss the use of conical crystals to extend the magnification range and improve the focusing efficiency compared to cylindrical crystals. Conical crystals provide for intercepting larger divergences than cylindrical crystals, with higher efficiency, better focus, and a range of magnifications from  $\sim 0.2$  to 2. In comparison with a toroidal mirror,<sup>14,15</sup> a conical crystal can intercept and focus a larger divergence and will introduce less mixing of the horizontal divergence into the vertical divergence.<sup>10,11,16</sup> In comparison with the meridional Johann and Johannson geometries,<sup>2,7,8</sup> the sagittal-conical crystal is better suited to tuning X-ray energy with fixed focus; it can be used with a first flat crystal to create a nondispersive system. Sagittal focusing also better preserves the perfect crystal rocking width; with meridional focusing, the crystal planes are also tilted in the diffraction plane and an incident ray intercepts the Bragg planes at various angles depending on the depth of penetration.<sup>17</sup> A related effect due to changing  $d$  spacing in a sagittal-elastically bent crystal is smaller by Poisson's ratio.

To illustrate the design restrictions imposed by the two-crystal, non-dispersive geometry, we briefly discuss the requirements for efficient diffraction of X rays. A crystal diffracts an X-ray beam only within a narrow energy bandpass,  $dE$ . The wavelength,  $\lambda$ , depends on the crystal plane spacing,  $d$ , and the incident angle,  $\theta_B$ , according to Bragg's law:  $2d\sin\theta_B = n\lambda$ . The width of the energy bandpass depends on the perfection of the crystal and the scattering strength of each plane. The intrinsic bandpass of a perfect crystal for  $\sigma$  polarized radiation (electric vector  $\perp$  to the scattering plane) can be estimated from

$dE/E \sim \frac{1.06}{\pi} \frac{e^2}{mc^2} N |F| (2d)^2 \sim 9.5 \times 10^{-25} N(\text{mm}^{-3}) |F| (2d(\text{nm}))^2$ , with  $N$  the number of unit cells/mm<sup>3</sup>,  $|F|$  the unit cell structure factor in electron units, and  $2d$  the usual Bragg plane spacing in nanometers.<sup>18</sup> For a nearly perfect Si<sub>111</sub> crystal reflection, the intrinsic bandpass  $dE/E \sim 1.5 \times 10^{-4}$ . The corresponding angular (Darwin) width can be calculated from  $\Delta\theta = \tan\theta dE/E$ . At 10 keV (1.6 eV) the Si<sub>111</sub> Darwin width is 0.03 mrad. An X-ray beam diffracting from two or more crystals must satisfy Bragg's law at each crystal for efficient diffraction. Though the energy bandwidth passed by two crystals is restricted by the bandpass of the first crystal, misalignment of the second crystal can lead to energy shifts in the intensity maximum by reflection of the weak Lorentzian tail of the bandpass from the first crystal.

As shown in Fig. 1(a), each ray in a non-dispersive, two-crystal monochromator makes the same Bragg angle at both crystals when the crystal planes are parallel. X rays diffracted from the first crystal will then be diffracted from the second crystal. The exit beam is parallel to the incident beam and can be held fixed in space as X-ray energy is tuned.<sup>19</sup> This nondispersive geometry does not allow for crystal focusing in the meridional (scattering) plane [Fig. 1(b)] except with graded d-spacing optics or for extremely small divergences. As illustrated in Fig. 1(b), curvature of the first (or second) crystal in the scattering plane causes a mismatch in the Bragg angles for rays with divergence,  $\delta$ , from the central ray in the meridional plane. The mismatch depends on the radius of curvature and on the magnitude of  $\delta$ . For synchrotron radiation with a vertical opening angle of about 0.2 mrad, only 2 to 10% of the vertical divergence can pass an  $M = 1$  monochromator as illustrated in Fig. 1(b). It is for this reason that the second curved crystal must act as a flat crystal in the meridional plane. Both cylindrical and conical crystals have this attribute as illustrated in Fig. 1(a).

Conical shapes have a practical advantage in that, like cylinders, they can be formed by bending flat plates. This simplifies the fabrication of an energy-tunable, fixed-exit, two-crystal monochromator such as demonstrated for the cylindrical curvature.<sup>11</sup> The four-point-bending scheme for creating cylindrical crystals can be used to create the slightly more complicated, conical shapes.

The conical crystal geometry is especially well suited to intercepting and focusing the 10 to 15 mrad horizontal fans of radiation typical of synchrotron radiation. Considerations of heat load, fixed focal spot, energy tunability, and divergence mixing dictate that the sagittal-focusing crystal should follow (be downstream of) a flat crystal.

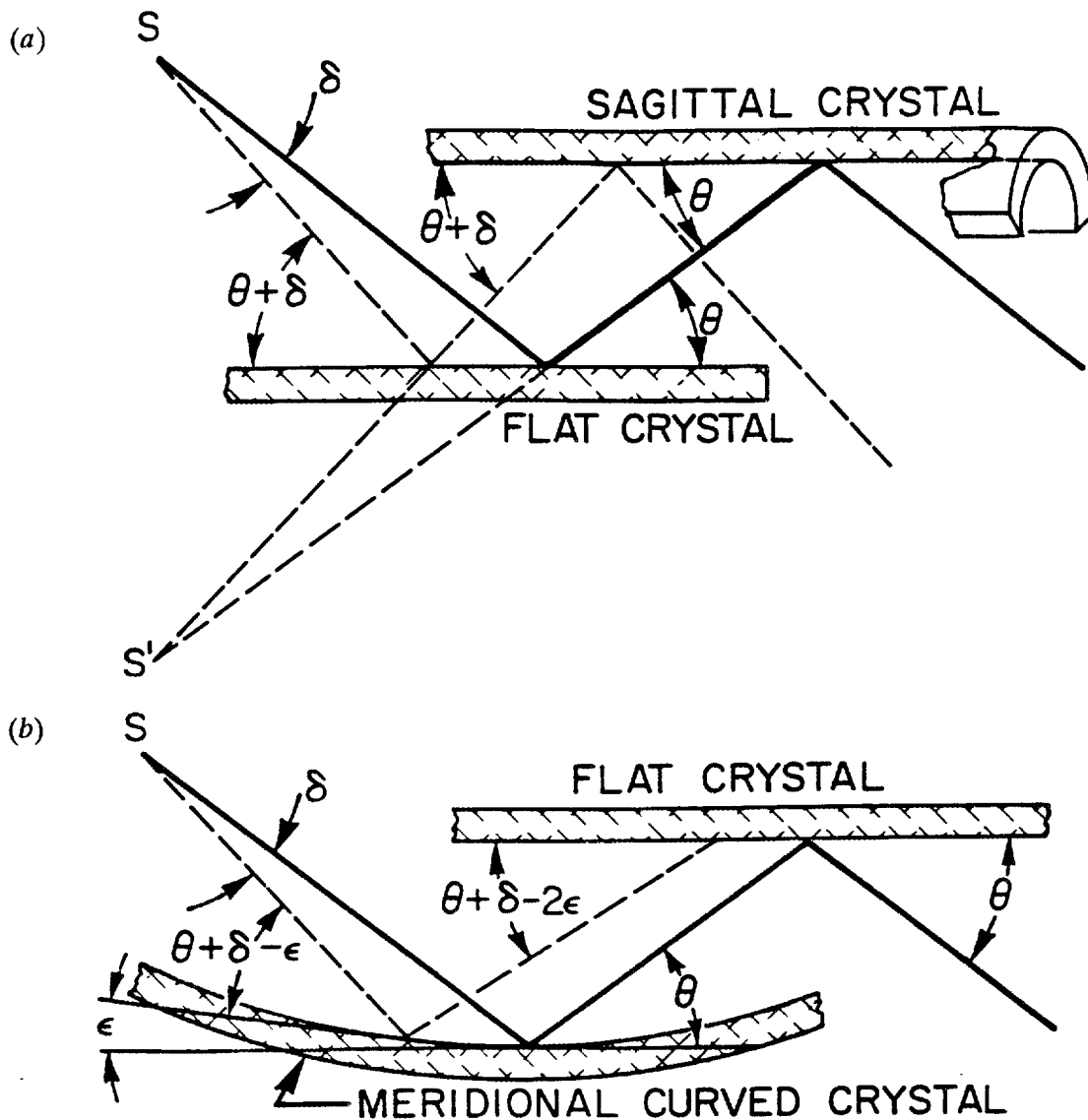


Fig. 1. (a) Diagram of nondispersive X-ray optics with a source divergence  $\delta$  in the scattering (meridional) plane. The central ray diffracts with Bragg angle  $\theta$  on both parallel crystals. A ray with meridional divergence  $\delta$  from the central ray diffracts with angle  $\theta + \delta$  on both crystals. The energy diffracted along the two ray paths differs according to Bragg's law. (b) A nondispersive arrangement with one crystal bent for meridional focusing. With the first crystal bent to the Johann or Johannson geometry for focusing, only the central ray makes the same Bragg angle on both crystals. The magnitude of the angular difference between the Bragg angles on the first and second crystal depends on the divergence from the central ray,  $\delta$ , and the radius of curvature.

## 2. CRYSTAL VERSUS MIRROR FOCUSING

X rays are usually focused either with total-external reflection from super-polished mirrors or by Bragg reflection from crystals.<sup>20</sup> For a given X-ray energy,  $E$ , total external reflection occurs when the angle of reflection,  $\theta$ , is less than a critical angle,  $\theta_c$ . The largest critical angles are for heavy element-coated mirrors where  $\theta_c(\text{rad}) \sim 0.08/E(\text{keV}) = 0.013/E(\text{fJ})$ . In comparison, the Bragg angle,  $\theta_B$ , for  $\text{Si}_{111}$  is 25 times larger;  $\theta_B \sim 1.976/E(\text{keV}) = 0.316/E(\text{fJ})$ . If we ignore absorption of the radiation, total external reflection at fixed scattering angle,  $\theta \leq \theta_c$ , allows glancing angle X-ray mirrors to act as low-pass X-ray filters; they reflect X-ray energies below a cutoff. In comparison, crystals only reflect a narrow energy band at Bragg scattering angles. With crystals, the diffracting Bragg planes need not be parallel to the crystal surface, which offers an additional degree of freedom.

Geometries for focusing with either X-ray mirrors or crystals are similar and well understood.<sup>1, 3, 14, 15, 20, 21</sup> A typical geometry is shown in Fig. 2. Curvature transverse to the plane of scatter causes sagittal focusing [Fig. 2(a-c)]. Focusing in the plane of scatter is called meridional focusing [Fig. 2(d)]. X rays can be doubly focused by a single optical element as in Fig. 2 or by sequential focusing in perpendicular planes, e.g., Kirkpatrick-Baez<sup>21</sup> (KB).

A practical focusing design for 3 to 8 keV (0.5 to 1.3 fJ) photons from a synchrotron radiation source is a toroidal mirror as described by Howell and Horowitz<sup>14</sup> and illustrated in Fig. 2. Focus is achieved when the mirror curvatures are given by:

$$R_s = \frac{2F_1F_2\sin\theta}{(F_1+F_2)}, \quad (1)$$

and

$$R_m = \frac{2F_1F_2}{(F_1+F_2)\sin\theta} = \frac{R_s}{\sin^2\theta}. \quad (2)$$

Here  $R_s$  is the sagittal radius of curvature and  $R_m$  is the meridional radius of curvature. Besides converging the radiation toward the central ray, the mirror deflects the central ray by an amount  $2\theta$ , absorbs X rays above the critical energy, and mixes horizontal divergence into the vertical divergence [Fig. 2(c)]. As illustrated in Fig. 2, the minimum mirror size to intercept radiation with a horizontal divergence,  $2\psi$ , and a vertical divergence,  $2\delta$ , is  $2F_1\psi$

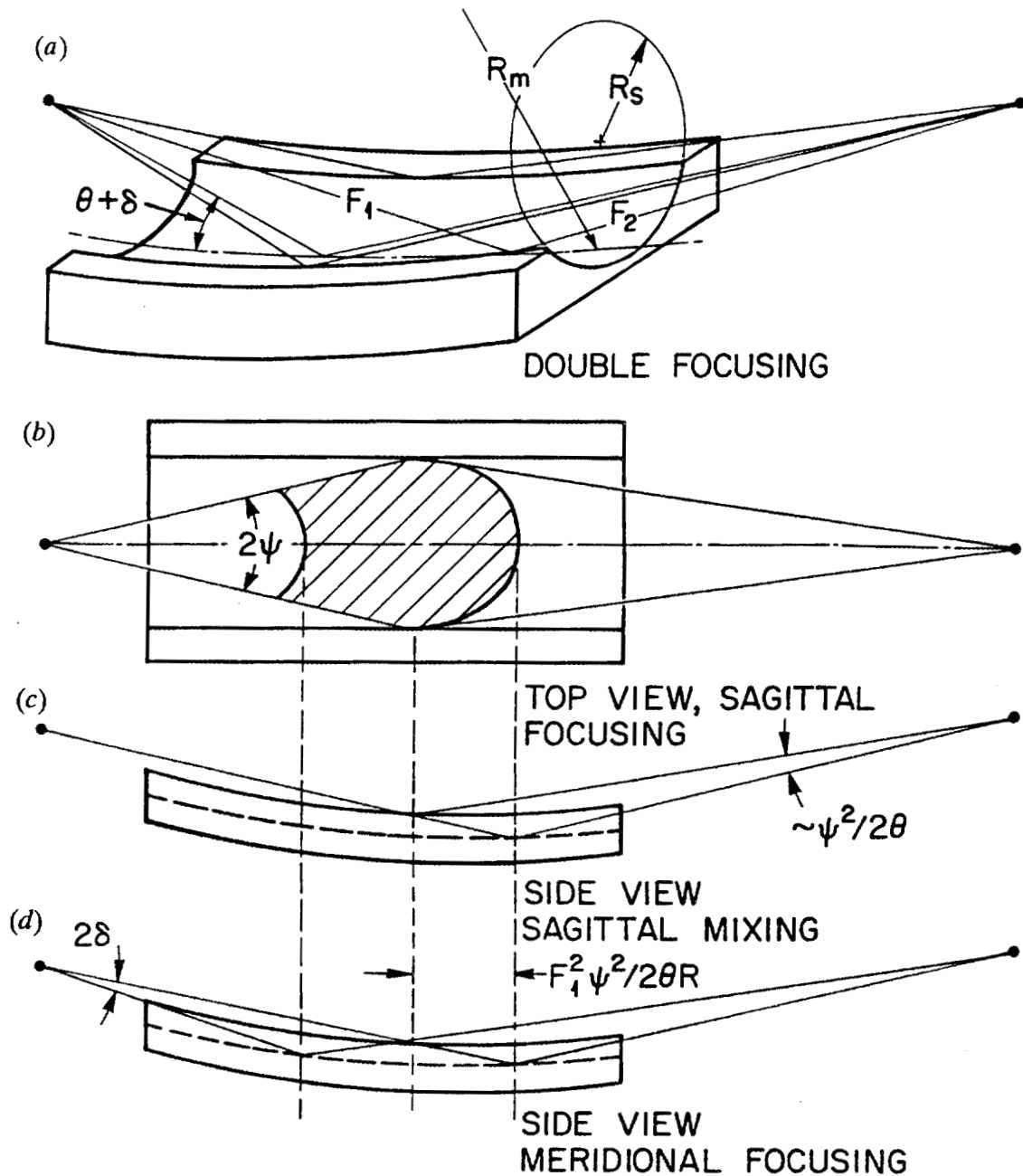


Fig. 2. (a) Geometry of doubly focusing X-ray optic:  $F_1$  source to optics distance,  $F_2$  optic to image distance,  $R_s$  the sagittal curvature, and  $R_m$  the meridional curvature. The central ray is reflected with an angle  $\theta$ . (b) Top view showing sagittal focusing with the characteristic smile of the beam intercept on the curved surface. (c) Side view of sagittal focusing shows how sagittal focusing must mix the sagittal divergence into the meridional divergence to maintain a good focal spot. (d) In-plane or meridional focusing with meridional curvature  $R_m$ . Since  $R_m = R_s/\sin^2\theta$ , the curvature required for in-plane focusing is much less than for sagittal focusing, especially at glancing angles.

wide by  $(2F_1\delta/\theta) + (F_1^2\psi^2/2\theta R_s)$  long. The  $\psi^2$  term arises from the horseshoe-shaped intercept of the horizontally divergent beam on the sagittally curved mirror surface as shown in Fig. 2(b).<sup>14-16</sup> This intercept shape is the same for a sagittally curved crystal.<sup>10</sup> As illustrated in Fig. 2(c), the radiation scattered from the trough and sides of the mirror (or crystal) must result in some mixing of the horizontal divergence into the vertical beam convergence for point focusing. The increase in vertical divergence is roughly  $\psi^2/2\theta$  for  $M = 1$ . Since a crystal reflects 10-keV (1.6-fJ) X rays at Bragg angles,  $\theta_B$ , which are about 25 times larger than for mirror reflections, the mixing of the horizontal divergence into the vertical is 25 times less for sagittal crystal focusing. For a point-focusing X-ray mirror with 10-mrad glancing angle, mixing of the horizontal into the vertical divergence will begin to dominate the nominal 0.2-mrad vertical divergence when  $\psi \geq 2$  mrad.

A way to avoid mixing the horizontal divergence into the smaller vertical divergence is to use a KB focusing arrangement.<sup>21</sup> In this geometry, two crossed meridional focusing mirrors or crystals are used. The complexity of configuring two separate optics as energy is tuned is primarily justified when large demagnifications are required. The KB design also has limited angular acceptance. With Eqs. (1) and (2), it can be shown that the sagittal geometry can focus radiation with a larger divergence than the meridional geometry. At unit magnification, the length of optic required to intercept a divergence  $2\psi$  with sagittal focusing is  $\sim F_1\psi^2/2\theta^2$ . The length of optic required to intercept the same divergence with meridional focusing is  $\sim F_12\psi/\theta$ , which is  $4\theta/\psi$  times longer. To focus a divergence  $2\psi = \theta/2$ , a meridional optic must be 16 times longer than a sagittal optic. Meridional X-ray mirrors with glancing angles  $\leq 10$  mrad must be  $\geq 0.5$  m to collect beams  $\geq 5$  mm high in the meridional plane. Such mirrors challenge the art of mirror fabrication.

Several synchrotron radiation beamlines have used meridional-focusing crystals that can be built to collect beams several millimeters wide.<sup>7,8</sup> These optics have energy tunability limited by the motion of the focal spot as energy changes and by the limited energy range set by the asymmetric cut required for good focus when  $M \neq 1$ . A further disadvantage is their incompatibility with a double-crystal, nondispersive geometry for fixed exit beam [Fig. 1(b)]. In the nondispersive configuration, a curved meridional-focusing crystal must be followed by a curved-defocusing crystal to ensure that each ray makes the same Bragg angle on the second crystal as on the first.

### 3. CONICAL CRYSTAL GEOMETRY

Tunability with crystal-focusing optics necessitates changing Bragg angle and curvature [Eq. (1)], which dictates simplicity in design. The simplest shape for a sagittal-focusing element is a cylindrically curved surface, and the next is a cone as shown in Fig. 3. It has been shown<sup>10</sup> (corrected here for an omission of the exponent 2 on  $\tan^2\psi$ ) that a line of sagittally divergent rays from a point source intercepts a cylindrical surface at angles  $\theta_S$  given by:

$$\sin\theta_S = \sin\theta_B \sqrt{\frac{1 + \alpha \tan^2\psi}{1 + \tan^2\psi}}, \quad (3a)$$

where

$$\alpha = \frac{2F_1}{N\sin\theta_B} - \left[ \frac{F_1}{N} \right]^2. \quad (3b)$$

With reference to Fig. 3,  $N$  is the cylindrical bend radius,  $\theta_B$  is the Bragg angle of the central ray,  $\psi$  is the sagittal divergence (horizontal for most synchrotrons) from the central ray, and  $F_1$  is the source to crystal distance. When  $N = F_1 \sin\theta_B / (1 \pm \cos\theta_B)$ , then  $\alpha = 1$  and  $\sin\theta_S = \sin\theta_B$  for all  $\psi$ .<sup>10</sup> This important relationship has two solutions:  $N \sim \infty$  ( $1 - \cos\theta_B$  solution) and  $N \sim F_1 \sin\theta_B / 2$  ( $M \sim 0.33$ ;  $1 + \cos\theta_B$  solution). Hence, cylindrically curved crystals that are nearly flat or bent for  $M \sim 0.33$  will diffract a fan of radiation at nearly constant Bragg angles independent of  $\psi$ . This is also true for total external reflection mirrors.

Rays from a fan of radiation with divergence  $2\psi$  intercept a flat crystal at angles varying from  $\theta_B$  for the central ray to  $\theta_\psi$  given by  $\sin\theta_\psi = \sin\theta_B \cos\psi$ . Thus, when following a first flat crystal, a second crystal has highest efficiency if it compensates for the small  $\psi$  dependence of  $\theta_\psi$ . For example, the second crystal should not be curved to the nearly flat solution ( $1 - \cos\theta_B$ ) but should be identically flat as is well known. A slight curvature of the first crystal to the ( $1 - \cos\theta_B$ ) solution would narrow the energy band passed by the monochromator; the effect is only about 0.5 eV (0.08 aJ) at 10 keV (1.6 fJ) and  $2\psi = 20$  mrad.

Away from the condition  $M \sim 0.33$ , a fan of X rays diffracted from a first flat crystal will not, in general, make the same Bragg angles on a cylindrically curved crystal for sagittal focusing. To determine the next step in configuring the crystal, we expand Eq. (3) in  $\psi$ .

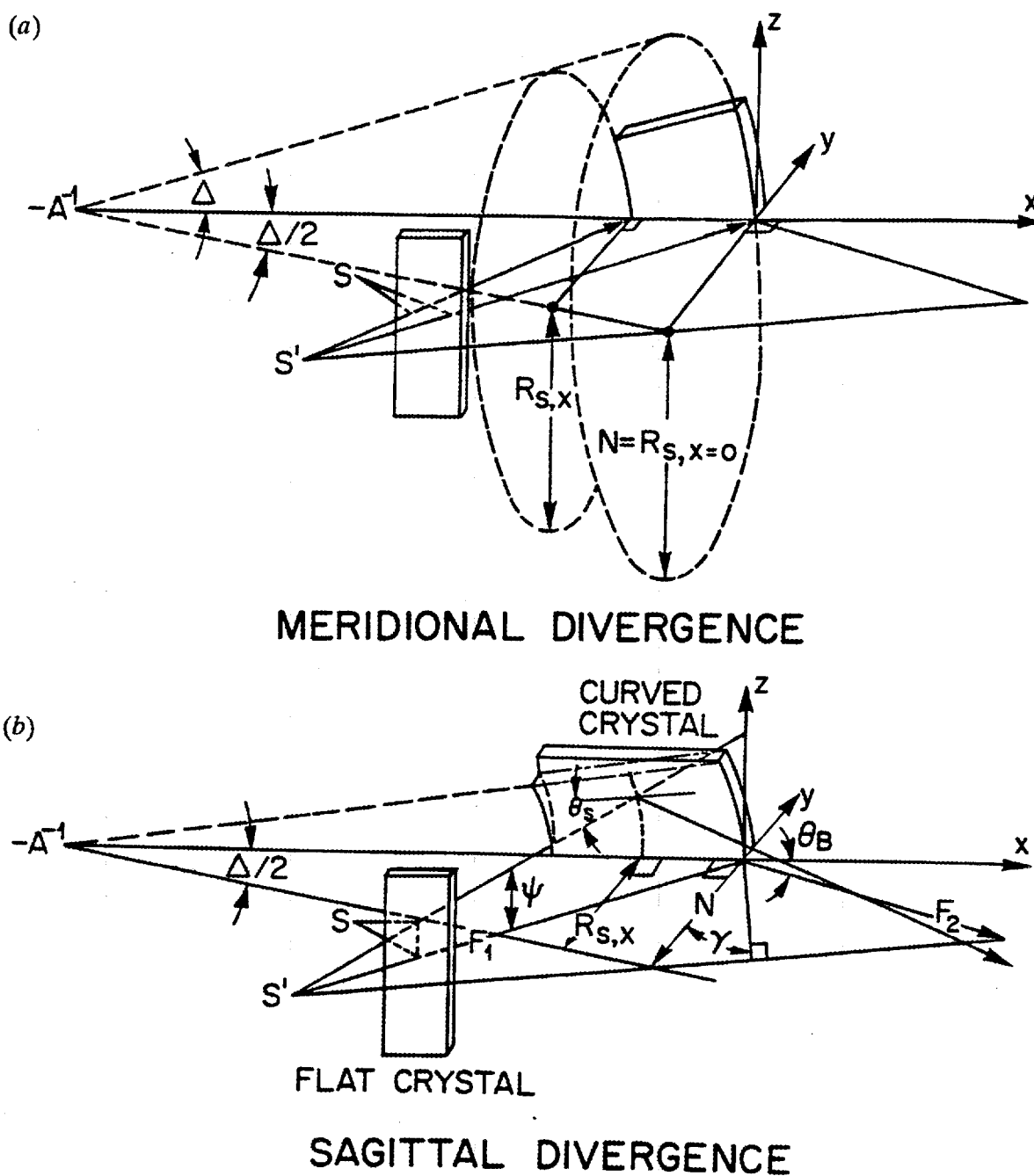


Fig. 3. (a) Geometry for the conical or cylindrical-crystal flat-crystal nondispersive monochromator. In the meridional (scattering) plane, the bent crystal acts as a flat crystal to the first flat crystal in the nondispersive geometry. (b) Geometry for determining the angle  $\theta_C$  of a ray with horizontal divergence  $\psi$  striking a conical surface.

Tan $\psi$  is small ( $\psi \sim 1$  to 10 mrad) compared with  $\sin\theta_B$ , ( $\theta_B \sim 100$  to 1000 mrad) for the usual crystal lattice spacing. It is a good approximation that  $\psi < \sin\theta_B$ . With the approximation

$\sqrt{1+\delta} \sim 1 + \frac{\delta}{2}$ , Eq. (3a) reduces to the form:

$$\sin\theta_s \approx \sin\theta_B - \frac{\sin\theta_B \tan^2\psi}{2} + \frac{\alpha \sin\theta_B \tan^2\psi}{2}. \quad (4)$$

For  $\theta_s$  to precisely equal  $\theta_B$ , the last two terms must be made to cancel. However, as discussed above, the angles  $\theta_\psi$  of rays in a fan of radiation incident on a flat crystal vary with the horizontal divergence  $\psi$  as:

$$\sin\theta_\psi = \sin\theta_B \cos\psi \approx \sin\theta_B - \frac{\sin\theta_B \tan^2\psi}{2}. \quad (5)$$

Since the first two terms of Eqs. (4) and (5) are the same, we need only make the third term of Eq. (4) negligible for the highest diffraction efficiency through a flat-crystal-sagittal-crystal pair. The angle  $\theta_\psi$  is nearly equal to  $\theta_B$ . For example, for  $\text{Si}_{111}$  or  $\text{Ge}_{111}$ ,  $\theta_\psi$  differs from  $\theta_B$  by only 0.01 mrad for 10 keV (1.6 fJ) X rays when  $2\psi = 20$  mrad and by  $6 \times 10^{-4}$  mrad for 40 keV (6.4 fJ) X rays when  $2\psi = 10$  mrad.

We look for a solution to Eq. (4) that makes the third term negligible. For arbitrary curvature  $N$ , the third term in Eq. (4) can represent a serious mismatch in the Bragg angles of rays reflected from a first flat-crystal incident on a sagittally focusing cylindrical crystal. For example, at  $M = 1$ ,  $N = F_1 \sin\theta$ ; hence,  $\alpha = 1/\sin^2\theta_B$  and Eq. (4) reduces to:

$$\sin\theta_s \approx \sin\theta_B - \frac{\sin\theta_B \tan^2\psi}{2} + \frac{\tan^2\psi}{2\sin\theta_B}. \quad (6)$$

Efficient transmission at  $M = 1$  for an  $\text{Si}_{111}$  flat-crystal-cylindrical-crystal pair occurs only when  $\psi \leq 0.005\theta$ , which is when  $2\psi$  is about 2 mrad for 10 keV (1.6 fJ) X rays.

We show that with a conical geometry, the third term in Eq. (4) is canceled to first order by a term that includes the cone angle,  $\Delta$ , which is defined in Fig. 3. If the crystal bend

radius,  $R_{S,X}$ , changes along the length of the crystal as in Fig. 3, then the crystal surface defined by the coordinates X, Y, and Z is given by:

$$Y = R_{S,X} \left( 1 - \sqrt{1 - (Z/R_{S,X})^2} \right),$$

where

$$R_{S,X} = N(1 - AX) \quad (7)$$

As shown in Fig. 3,  $X = 0$  is defined as the X intercept of the central ray on the conical crystal, and  $R_{S,X} \geq N$  for A and X positive. The apex of the cone is located at  $X = -A^{-1}$  [Fig. 3(a)] and may be toward the source ( $A > 0$  for  $M > 0.33$ ) or toward the focus ( $A < 0$  for  $M < 0.33$ ). For  $Z \sim F_1 \tan \psi$  small, the conical-crystal surface has a slope in the scattering plane that grows as  $Z^2$ . We differentiate Eq. (7) to find the slope of the conical surface as a function of Z along the X-axis. The angle,  $\theta_s$ , for a ray with horizontal divergence  $\psi$ , which intercepts the conical surface of Fig. 3, is then given by:

$$\sin \theta_s \sim \sin \theta_B - \frac{\sin \theta_B \tan^2 \psi}{2} + \frac{\alpha \sin \theta_B \tan^2 \psi}{2} - \frac{AF_1^2 \tan^2 \psi}{2N} \quad (8)$$

If the last two terms of Eq. (8) are made to cancel, then the first two terms of Eq. (8) match the flat-crystal case given in Eq. (5). The condition for canceling the last two terms is given by:

$$A = \frac{\alpha N \sin \theta_B}{F_1^2} = \frac{3M - 1}{2F_1 M} \quad (9)$$

At unit magnification  $A = 1/F_1$ , and the crystal is configured to a cone with cone length  $F_1$  [Fig. 3(a)]. At  $M = 0.33$ ,  $A = 0$  and the special cylindrical case is realized.<sup>10</sup> In general, by following the prescription of Eq. (9), it is possible to intersect a horizontal fan of radiation and reflect it first off a flat crystal, then condense the radiation with a conical crystal over a useful magnification ranging from 2 to 0.2. This range is limited primarily by increased focal aberrations and reduced transmission for finite source size. The cone angle in degrees for

Si<sub>111</sub> at 10 keV (1.6 fJ) is plotted in Fig. 4 as a function of magnification. The cone angle  $\Delta = \arctan(2R_{S,X=0}A)$  depends only on magnification and Bragg angle:

$$\Delta = \arctan\left[ \frac{6M-2}{1+M} \sin\theta_B \right] . \quad (10)$$

Also plotted in Fig. 4 are the radii,  $R_{S,X=0} = N$  for Si<sub>111</sub>,  $E = 10$  keV (1.6 fJ),  $F_1 = 20$  m, and  $F_1 + F_2 = 40$  m. At  $M \sim 1$ , the crystal radius  $R_{S,X}$  is a maximum for a fixed source-to-image distance. In the next section, focal aberrations are also shown to be minimized near  $M = 1$ .

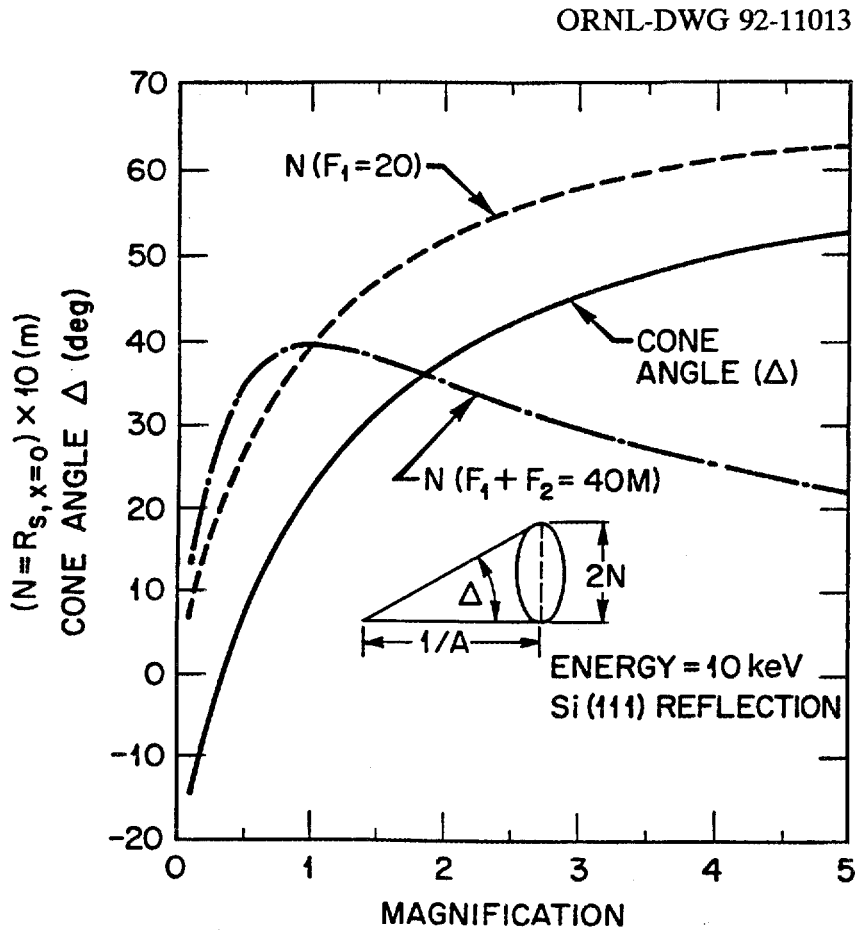


Fig. 4. The cone angle  $\Delta$  as a function of magnification  $M$ . At  $M \sim 0.33$ , the cone angle goes from negative to positive. Also plotted are the sagittal focusing radii,  $N = R_S = 2MF_1 \sin\theta / (1+M)$ , as a function of  $M$  for  $F_1 = 20$  m and for  $F_1 + F_2 = 40$  m. Note that the radii are multiplied by a factor of 10 to put them on the same scale as the cone angle  $\Delta$ .

#### 4. RAY-TRACING RESULTS

A Monte-Carlo ray-tracing program was used to study the imaging and transmission efficiency of the conical crystal geometry. A study of focusing aberrations and efficiency with cylinders and a point source has been given.<sup>10</sup> Ray tracing allows a generalization to finite source size and conical shapes. A white-beam Gaussian source was assumed with adjustable vertical and horizontal spatial distributions. The spatial and angular distributions were chosen to model a second-generation synchrotron radiation source [National Synchrotron Light Source (NSLS)] or a third-generation source [Advanced Photon Source (APS)]. The vertical divergence was Gaussian. A uniform horizontal intensity with a divergence of up to 15 mrad was assumed as might result from a simple slit system on a bend magnet or wiggler synchrotron radiation source. The transmission for each ray was estimated from the Darwin width overlap of the two crystal reflections. Unit efficiency was assumed when the Bragg angles were identical at both crystals. A cylindrical specular-reflecting mirror for meridional focusing of the vertical divergence was modeled upstream of the crystal pair. A cylindrical mirror upstream has negligible aberration for focusing the vertical divergence and avoids the increased vertical divergence from the flat-crystal-conical-crystal pair. A schematic of the modeled focusing optics is shown in Fig. 5. For the calculations presented below, the mirror was modeled at 1 m upstream of the focusing crystal.

The focusing aberrations were first studied assuming a negligibly small source. The size of the image was calculated for various horizontal divergences, energies, magnifications, and focal distances. The aberrations were found to be a minimum near  $M = 1$ . In Fig. 6, the vertical and horizontal aberrations are compared as a function of magnification at 10 and 30 keV (1.6 and 4.8 fJ). The most serious focusing errors are in the scattering plane. The RMS image size is calculated with  $F_1 = 30$  m and  $2\psi = 6$  mrad. As illustrated, the aberrations are minimized near  $M = 1$ .

The introduction of finite horizontal source size reduces the focusing efficiency of both the  $M = 1$  and  $M = 0.33$  geometries. The cylindrical  $M = 0.33$  case is more sensitive to source size and has less transmission from an extended source than does the  $M = 1$  geometry. The relative merits of sagittal-crystal focusing at various magnifications depend on the goals for the focusing optics and the source properties. With large sources, it is possible to obtain smaller images by using demagnifying optics. Increased focused intensity results as long as the demagnified image size is small compared to the focusing aberrations. Demagnifying optics,

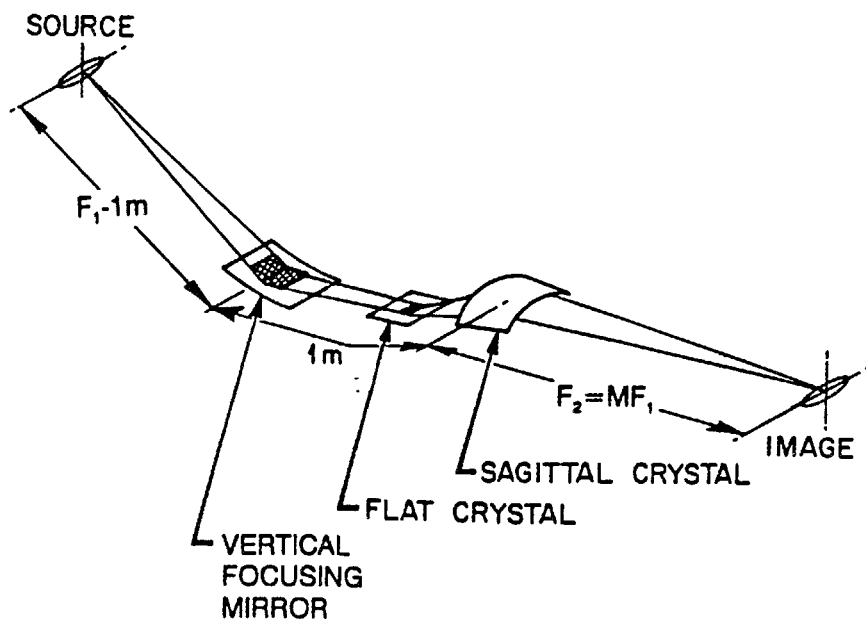


Fig. 5. Modeled optical geometry used in the ray-tracing calculations of the conical crystal focusing. The in-plane (meridional) focusing mirror is used to focus the small vertical synchrotron radiation divergence. The sagittal focusing crystal is used to collect and focus 15 mrad of synchrotron radiation divergence. Ray-tracing programs are particularly useful for studying the effect of source size on focusing performance.

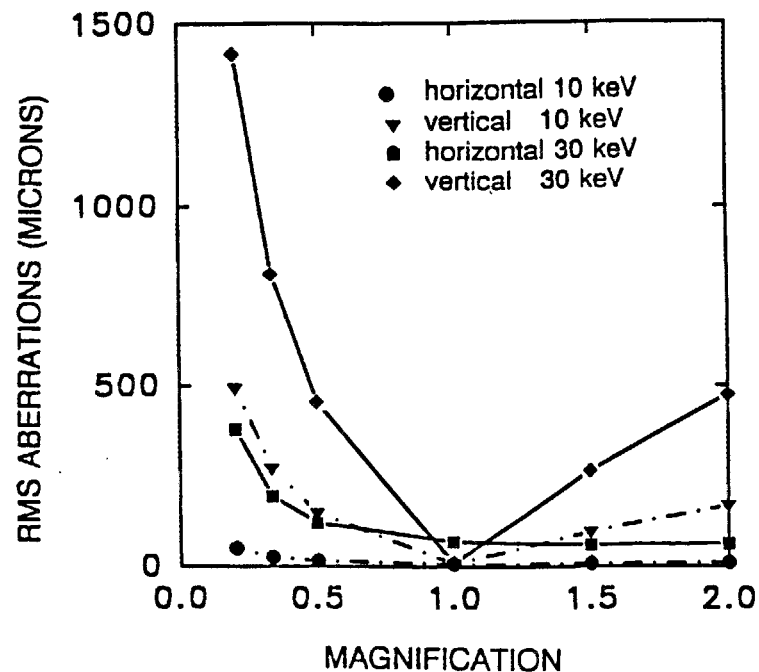


Fig. 6. RMS image size for a 10 or 30 keV (1.6 or 4.8 fJ) x-rays from a point source with 6 mrad horizontal divergence focused by a conical crystal ( $F_1 = 30\text{ m}$ ). Both horizontal and vertical RMS image sizes are plotted as a function of magnification.

however, increase the beam divergence at the image. For a realistic comparison between the cylindrical ( $M = 0.33$ ) and conical ( $M = 1$ ) shapes, a root-mean-square (RMS) source size of 0.31 mm horizontal by 0.085 mm vertical was assumed. This source size is near that anticipated for a wiggler on the third-generation APS.<sup>22</sup> As shown in Fig. 6, the focal aberrations are about an order of magnitude less for  $M = 1$  than for  $M = 0.33$ , but the geometrical image area is almost an order of magnitude less in the  $M = 0.33$  case. Though the total flux passed with  $M = 1$  is comparable to the total flux passed with  $M = 0.33$ , the geometrical intensity gain expected for  $M = 0.33$  is not fully realized. As shown in Fig. 7, the focused intensity through a 200- $\mu\text{m}$ -diam pinhole can be 3 times higher for  $M = 1$  than for  $M = 0.33$ . The  $M = 1$  geometry outperforms the  $M = 0.33$  cylinder above  $\psi = 2$  mrad.

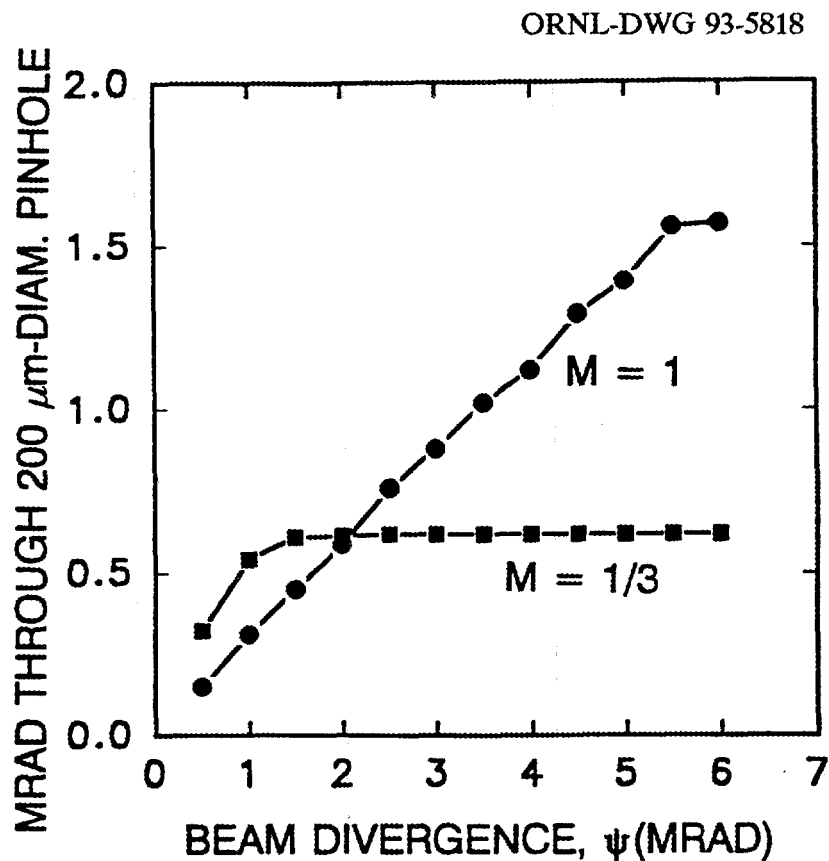


Fig. 7. Comparison of the transmission through a 200- $\mu\text{m}$ -diam pinhole with  $M = 0.33$  and  $M = 1$ . For this comparison, the source size and vertical divergence are modeled after the anticipated parameters for a wiggler line at the APS (see text). The comparison is virtually identical for an APS bending magnet line.

$M = 1$  preserves the vertical height of the source much better than  $M = 0.33$ . Furthermore, the cylindrical crystal for  $M = 0.33$  must tolerate a greater stress as it is bent to a smaller radius, which for the same source-to-image distance,  $F_1 + F_2$ , is three-fourths the radius of the  $M = 1$  (conical) geometry. Also, for the same  $F_1 + F_2$ , the sagittal smile (Fig. 2) is three times larger for the cylindrical geometry than for the  $M = 1$  conical case.

The overall performance at  $M = 1$  is illustrated in Fig. 8, which shows the transmission and image size with  $F_1 = 10$  m and for an RMS source vertical and horizontal size of 0.4 by 0.05 mm<sup>2</sup>. A small, vertical source size was used in this ray-tracing calculation to again make the vertical focus sensitive to aberrations. The calculated focal spot size was sensitive to average curvature. Transmission was sensitive to the cone length  $A^{-1}$ , peaking at an  $A$  defined as in Eq. (9). Transmission efficiency was nearly identical to that expected for two flat crystals

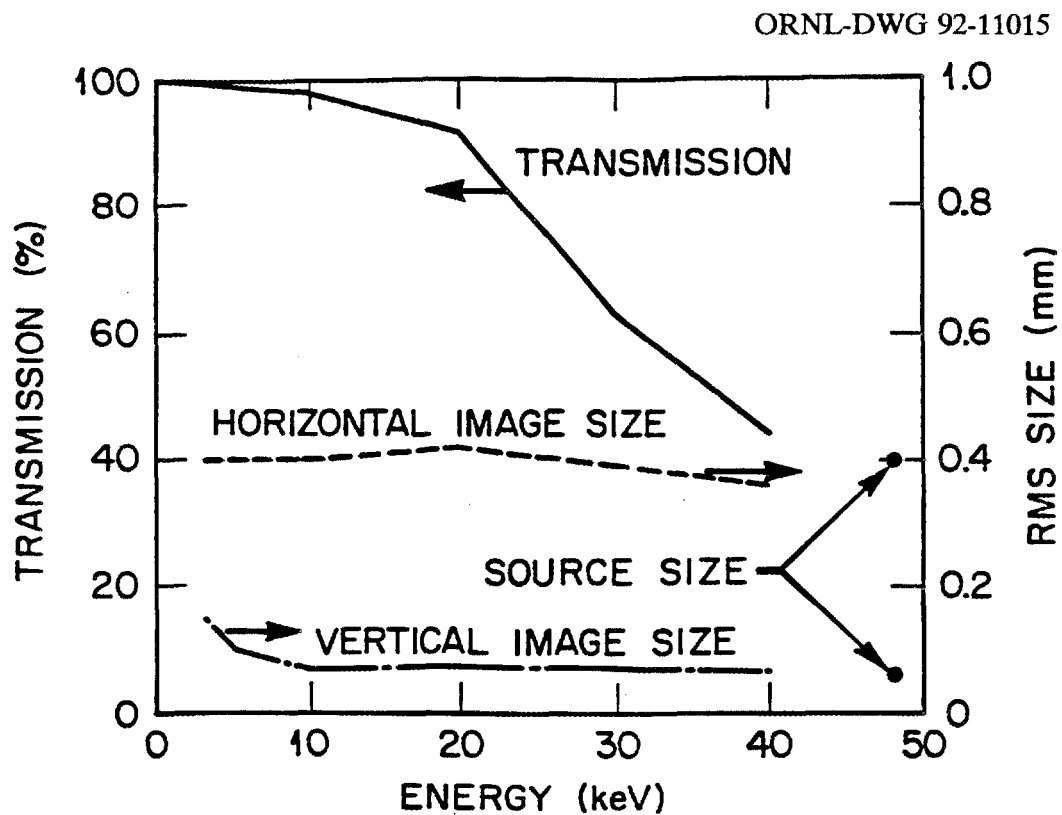


Fig. 8. Performance of the model focusing system of Fig. 5 for  $F_1 = 10$  m,  $M = 1$ , and  $2\psi = 15$  mrad. The crystals were assumed to be  $\text{Si}_{111}$ . The source was assumed to have an RMS horizontal and vertical size of 0.4 by 0.05 mm<sup>2</sup>. Decreased transmission at higher energies results from the inability of the focusing crystal monochromator to accept the full horizontal source size.

at lower energies but began to decrease at higher energies, dropping to one-half at 40 keV (6.4 fJ). The horizontal RMS image size became slightly less than the source size at high energies; rays originating from source points away from the nominal origin have reduced transmission through the flat-crystal-conical-crystal pair. This sensitivity to phase space accounts for most of the decrease in transmission with higher energy. Except for the very lowest energies, the RMS vertical focus is near the geometrical limit. Based on the ray-tracing results plotted in Fig. 7, a flat-crystal-conical-crystal nondispersive monochromator preceded with a vertical focusing mirror can achieve nearly ideal focusing at  $M \sim 1$ . Actual transmission efficiency will depend on the precision of the bending device and uniformity of the crystal shape and its elastic response. As discussed later, experience has shown that good transmission efficiency can be achieved.

## 5. ALIGNMENT AND OPERATION

### 5.1 BENDING MECHANISM

We have applied the conical-crystal design to our own beamline X14 at the NSLS.<sup>23</sup> This successful application routinely focuses  $\sim 5$  mrad from 3 to 25 keV (0.5 to 4 fJ) and has prompted others to follow. We describe the bending mechanism used at X14 as it contains the essential elements required to bend cylindrical and conical crystals.

The bender consists of four rods with two rods fixed by an optical plate to lie in a plane, and with the other two rods driven by four independent linear translators: one at each end (Fig. 9). The two fixed rods are parallel while the two movable rods operate in planes perpendicular to the plane defined by the fixed rods. This bending scheme can only approximate the conical shape defined by Eq. (7), but practice has shown that the errors are not significant. Previous experiments with a more complicated bender, which allowed a more precise bending of the crystal surface by pointing the two fixed rods toward the conical apex, did not improve the focus or X-ray transmission over that achieved with the simpler bender.<sup>11</sup> In the X14 design, the choice was made to translate the outer rods and keep the inner rods fixed (Fig. 9); this produces less displacement of the crystal center when bent.

The four-rod bender differs from a four-point bender in that the moments are applied along four lines that allow the opposing moments to change nearly linearly from the front to the back of the bent crystal. For simplicity, the four-point bender model is used to illustrate

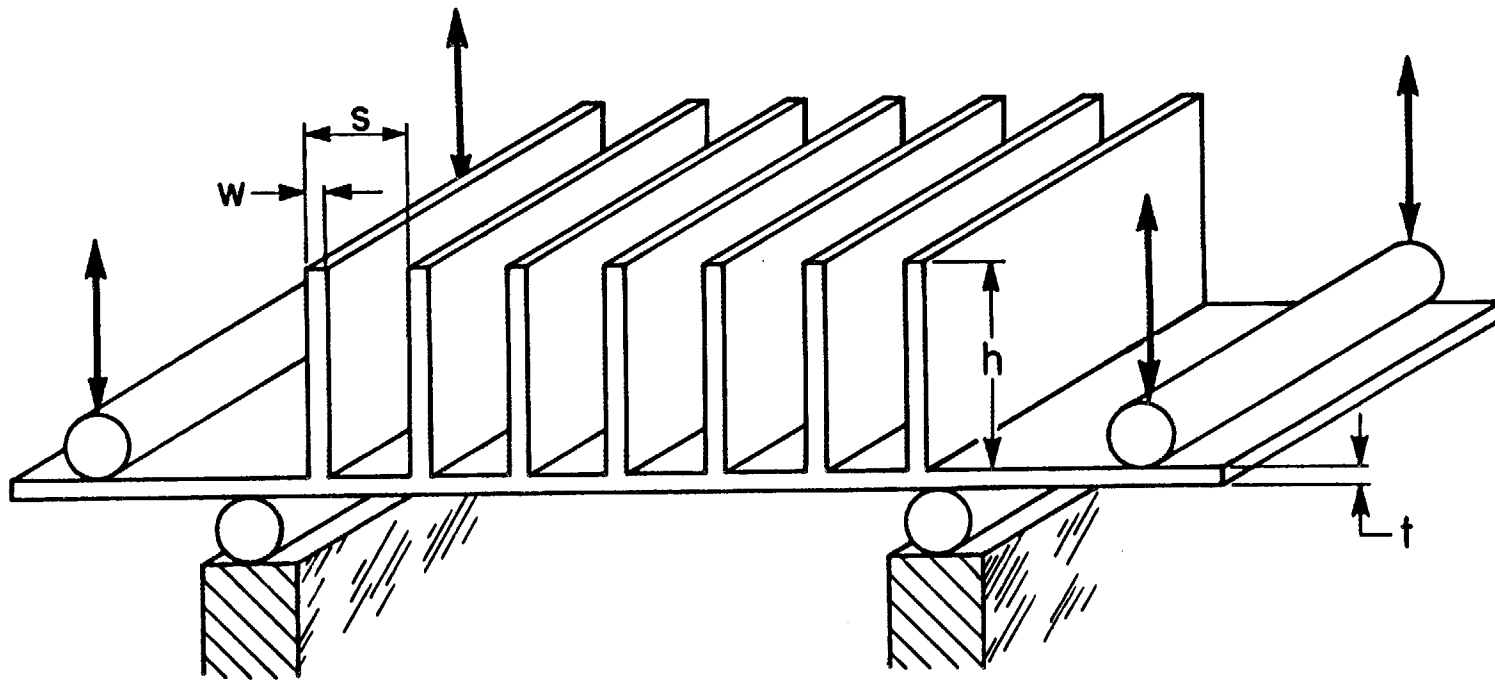


Fig. 9. Illustration of the four-rod-bending scheme and a ribbed crystal to suppress anticlastic bending. Two rods are fixed to an optically polished plate while the ends of the other two rods are independently controlled by stepping motors with submicron resolution. Designs where either the inside or outside rods are moved have been successfully tested.

the performance. Consider the four-point-loaded beam as shown in Fig. 10. The center supports are fixed and the end points are driven with force  $W_1$  and  $W_2$ . We assume an outer rod spacing of  $l$  and a spacing of  $C$  between the outer support points. The bending moment diagram is shown below the beam.<sup>24</sup> Adjustment of the displacements (forces) of the outer rods varies the bending moment across the beam and can be made to produce a uniform bending moment between the inner rods. In addition, the displacements can be used to compensate for non-uniform elastic response or other bending errors. When under symmetric moments, the beam between the center supports undergoes pure bending moments and is bent with a radius  $R = d^2X/d^2Z = YI/M$ . Here,  $Y$  is Young's modulus and  $I$  is the moment of inertia of the beam cross section. The displacement of the crystal center,  $F_C$ , for a uniform displacement,  $F_1$ , of the outer rods is given by:

$$F_C = F_1 \frac{3(2c-l)^2}{4c(3l-4c)} \quad (11)$$

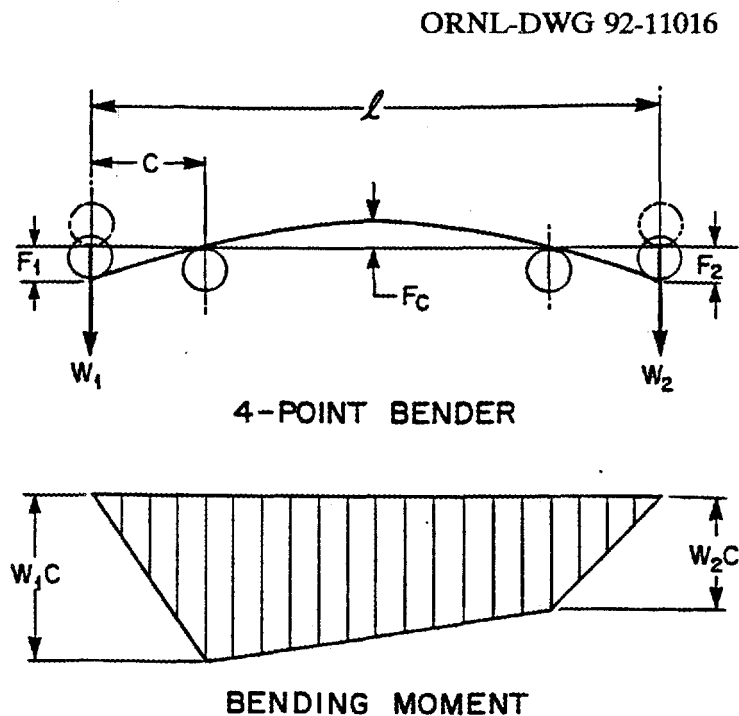


Fig. 10. Four-point-bending schematic for a uniform beam showing forces  $W_1$  and  $W_2$  applied at the outer points. The beam is bent by a displacement  $F_1$  from the relaxed beam at the end with force  $W_1$  and by  $F_2$  from the relaxed beam at the end with force  $W_2$ . The maximum central deflection is  $F_C$ . Below the four-point-bending schematic is the bending moment diagram. When  $W_1 = W_2$ , the displacements  $F_1 = F_2$  and the central portion of the beam experience a constant pure bending moment (no shear forces).

A conical shape with  $A > 0$  is achieved when the displacements of the rod ends near the source are made greater than the displacements nearest the focus. Since the rods are parallel, the constants  $C$  and  $l$  do not change along the length of the crystal, and displacements  $F_1$  and  $F_2$  retain a constant of proportionality. Cones with  $A < 0$  are configured with the relative displacements reversed. The displacement of the center of the crystal changes with the radius of curvature, as does the relative angle with respect to the first crystal. Both effects are small. A piezoelectric feedback circuit monitors the intensity throughput and compensates for relative Bragg angle change; computer-controlled motors move the entire bender up or down to compensate for the displacement,  $F_c$ , and to keep the exit beam fixed in space.

## 5.2 STIFFENING AGAINST ANTICLASTIC BENDING

The simple two-dimensional discussion does not account for the anticlastic response of a plate to bending. As a plate is bent in one direction, volume is approximately preserved by the development of a transverse (anticlastic) curvature as shown in Fig. 11 (ref. 25). For

ORNL-DWG 81-18578

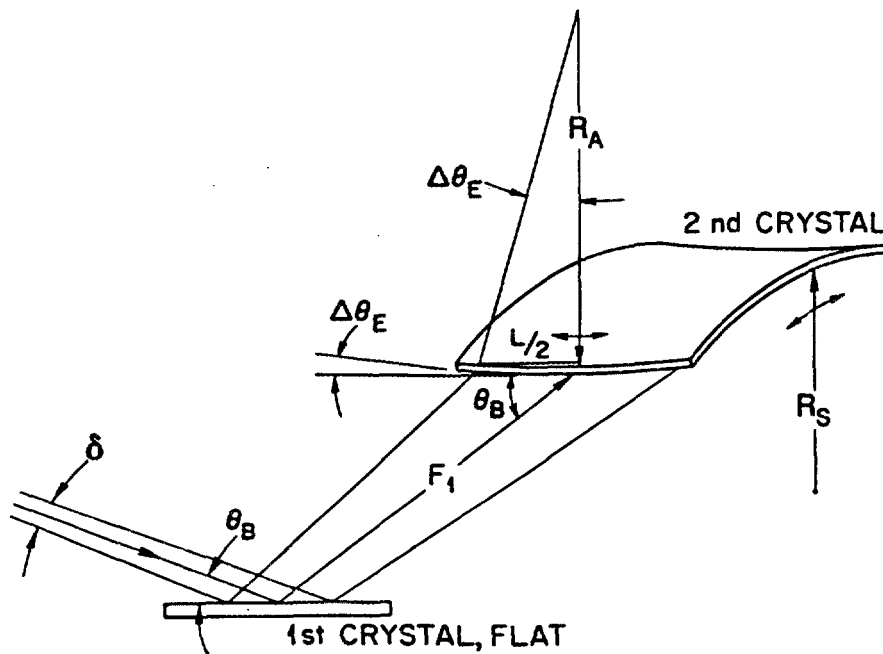


Fig. 11. An unsupported plate bent to a sagittal radius  $R_S$  develops an anticlastic curvature  $R_A$ , which is larger than  $R_S$  by the inverse of Poisson's ratio,  $\sigma$ , and produces an error  $\Delta\theta_E$  in scattering angle.

sagittally focusing crystals, the anticlastic curvature is in the meridional (Bragg scattering) plane and must be kept negligible to satisfy Bragg's law. From the elementary theory of elastically bent plates, an unsupported thin plate bent to a radius  $R_s$  takes on a transverse curvature  $R_A = R_s/\sigma$ .<sup>26</sup> Here,  $\sigma$  is Poisson's ratio, which is of the order of one-half to one-third. For  $\text{Si}_{111}$  and  $E > 5$  keV (0.8 fJ), the perfect crystal Darwin width is about  $1.5 \times 10^{-4} \sin\theta$ . If we assume  $\sigma = 0.5$ , then the meridional divergence  $\delta$  passed by an anticlastic, nondispersive two-crystal monochromator is very small;  $\delta \leq 3 \times 10^{-4} M \sin^3(\theta)/(1 + M)$ . This represents only a few percent of the vertical divergence from a synchrotron radiation source and greatly reduces the transmission efficiency similar to that shown in Fig. 1(b). We note that single-crystal silicon is highly anisotropic, and the anticlastic bending of Si wafers depends strongly on crystallographic orientation; single-crystal Si wafers with (100) surfaces show less anticlastic bending than Si wafers with (111) surfaces.

Anticlastic bending of the focusing crystal is suppressed with stiffening ribs<sup>11-13</sup> (see Fig. 9). These ribs have a small, deleterious effect on the uniformity of curvature for sagittal focusing but permit the crystal to be dynamically bent with negligible anticlastic bending. With stiffening ribs, the average meridional curvature  $R_m$  is approximately:

$$R_m = -\frac{N}{\sigma} \left[ 1 + \frac{w}{s-w} \left( \frac{h}{t} \right)^3 \right]. \quad (12)$$

Here,  $w$  is the rib width,  $s$  is the rib spacing,  $h$  is the rib height, and  $t$  is the plate thickness (Fig. 9). Typical dimensions are  $w = 0.5$  mm,  $s = 2.5$  mm,  $h = 10$  mm, and  $t = 0.5$  mm. With these dimensions, the average plate stiffness to anticlastic bending is increased by three orders of magnitude; this makes the meridional curvature negligible (one-fifth or less of the Darwin width) for X-ray energies up to 30 keV (4.8 fJ). The crystal thickness is limited by the fracture stress of the bent crystal. We chose  $t = 0.5$  mm to limit the stress on the outer surface of the Si crystal to about one-half the fracture stress for the smallest radius of curvature.

The focusing limits imposed by the ribbed crystal structure depend on the spacing,  $s$ , and width,  $w$ , of the ribs. We estimate the focusing blur due to the rib structure by averaging the blur from each segment of the crystal. Under each rib, the crystal is constrained to be nearly flat. The divergence of the radiation scattered from beneath the ribs is unchanged. If we assume that the average curvature of the crystal is correct, then the point-source focal

spot from each rib is  $(1 + M)w$ . Between the ribs, the radii must be smaller than the average crystal radius:  $R_{\text{Between}} = R_{\text{Average}}(1 - w/s)$ . The magnification  $M'$  for the segment between ribs is therefore **smaller** than the average magnification  $M$ ;  $M' = M(s - w)/(s + Mw)$ . The crystal overfocuses between the ribs and underfocuses at the ribs. Fortunately, the performance compromise is small for current generation sources. For example, with  $w = 0.5$  mm and  $M = 1$ , the underfocused spot size from beneath each rib will be 1 mm. With  $s = 2.5$  mm, the magnification  $M'$  is 0.66. For the focal spot at  $M = 1$ , the nominal 2-mm width of the beam intercepted between adjacent ribs is overfocused to 1 mm. We note that in a partially focused beam, a series of evenly spaced, brighter spots can be observed that arise from the overfocusing between the ribs. Rib width and spacing can be decreased to reduce the defocusing effect of the ribs.

### 5.3 ALIGNMENT OF MONOCHROMATOR

Proper alignment of the flat-crystal-conical-crystal pair is necessary to achieve near-ideal focusing and for a spatially fixed beam when scanning energy. The first flat crystal can be misaligned by a tilt  $\chi$  and by a displacement from the  $\theta$  axis of rotation of the monochromator [Fig. 11(a)]. The second crystal can be misaligned by a  $\chi'$  tilt, a  $\Delta\theta$  error, a crystal rotation  $\phi$ , and a sideways translation perpendicular to the plane of scatter [Fig. 11(a)]. To a first approximation, this sideways translation of the focusing crystal axis is equivalent to a  $\chi'$  tilt.

Alignment is made easier when both crystals are cut with their surfaces within  $0.25^\circ$  of being parallel to the diffracting planes. The crystals are then mounted and leveled with these surfaces within  $0.1^\circ$ . The first flat crystal is positioned with an optical telescope to lie with its surface at the center of the monochromator  $\theta$  rotation axis. The height of this  $\theta$  axis is then adjusted to intercept the raw X-ray beam at its center. The X-ray beam position on the surface of the first crystal can be observed by means of a fine dusting of fluorescent powder on the crystal.

The first alignment step with the X-ray beam is to determine the horizontal position of the optical axis at the focus. The simplest way is to observe the direct white beam at the focal plane. Shield restrictions often prevent this simple approach. Alternatively, the X-ray transmission is optimized with the relative  $\Delta\theta$  tilt, and the beam is approximately positioned horizontally with adjustment of the relative chi tilt  $\Delta\chi = \chi - \chi'$ , Fig. 12(a). Throughput is optimized with the second crystal unbent and with only a pencil X-ray beam  $\leq 0.2$  mrad in

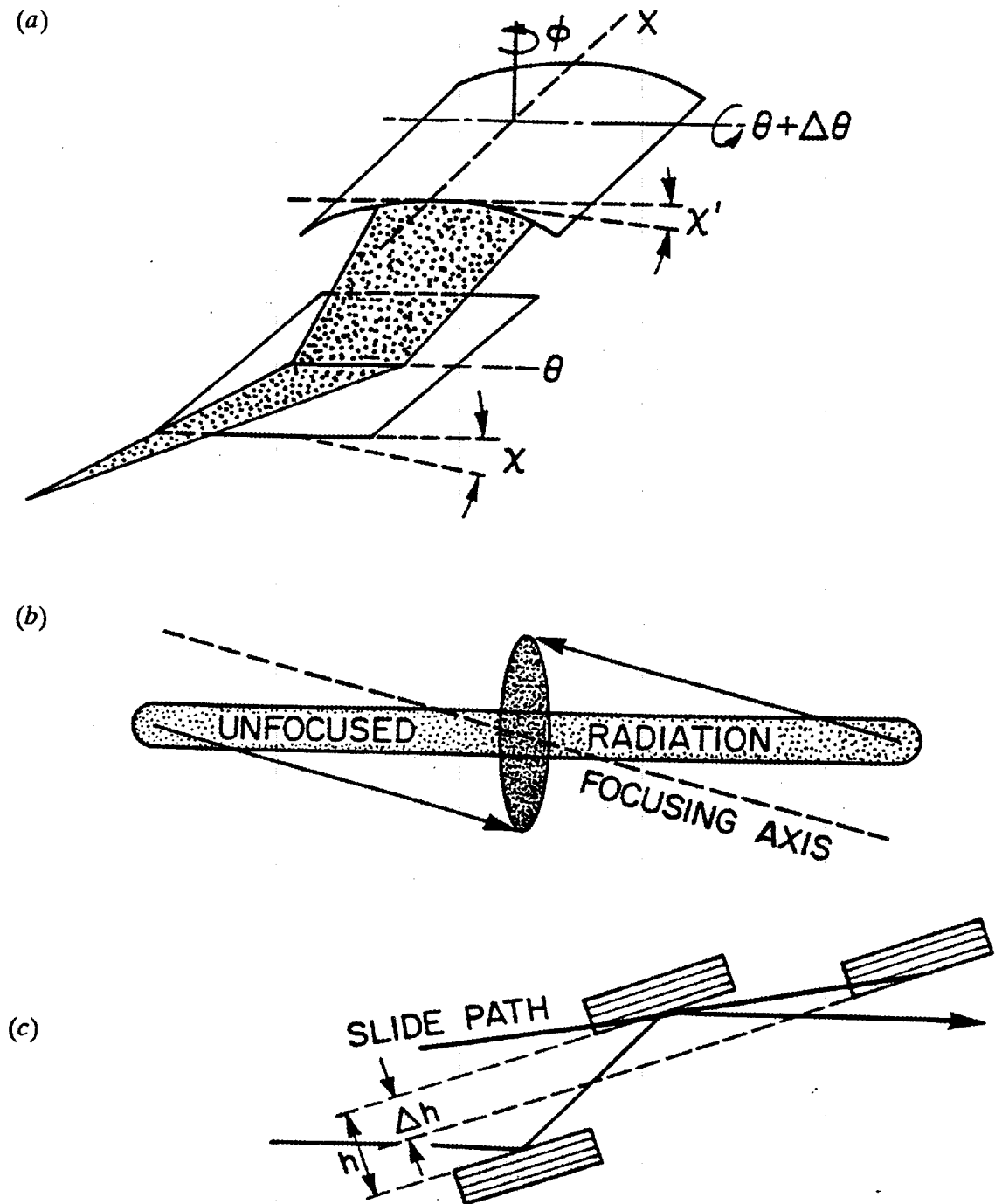


Fig. 12. (a) The alignment controls needed for the two-crystal monochromator include vertical displacement and  $\chi$ ,  $\theta$ , and  $\phi$  rotation axes. The two crystals can have a parallelism error in their chi tilt  $\Delta\chi$ . The crystal can also be rotated by  $\phi$ . (b) Unfocused and focused image when the scattering plane of the monochromator is not perpendicular to the plane of the storage ring. (c) Diagram showing how a misalignment of the horizontal translation axis for the linear slide results in a change in the crystal-crystal spacing,  $h$ , producing a vertical displacement of the beam as energy is scanned.

horizontal divergence around the central ray. The proper horizontal position for the focal spot of the beamline radiation is determined when the horizontal position of the diffracted beam does not change as a function of X-ray energy. With changing Bragg angle,  $\theta_B$ , the horizontal position is observed to move as  $2\Delta\chi\sin\theta_B$ . After a few iterations, the crystal planes are made parallel. The beam is observed during focusing to ensure that the  $\chi'$  tilt of the focusing crystal (and hence both crystals) lies parallel to the storage ring plane. As the beam is focused, even a small  $\chi$  tilt of the curved crystal relative to the ring plane is observed as an increase in the vertical focal spot size [Fig. 12(b)]. It is easy to align the tilt to within  $0.5^\circ$  by minimizing the vertical spot size. For fixed-exit operation, it is important that the Bragg planes be parallel to the axis of the linear slide used for translating the second crystal. The monochromator system incorporates a computer-controlled translation that allows the second crystal to maintain a constant intercept with the central ray [Fig. 12(c)]. Small errors in the parallelism of the crystal planes with respect to the linear slide are observed as displacement errors  $\Delta h$ , as a function of  $\theta_B$  [Fig. 12(c)]. Adjustments of the  $\theta$  tilts of both crystals make it possible to simultaneously maintain crystal parallelism and to make both crystal Bragg planes parallel to the linear slide.

As recognized by Kawata et al.,<sup>27</sup> the orientation of the conical/cylindrical axis X, in Fig. 12(a), must lie in the scattering plane of the beam [Fig. 12(c)]. Deviations  $\phi$ , in the rotation of this axis out of the scattering plane lessen beam transmission and increase the rocking curve width measured for the curved crystal.<sup>28</sup> The angular error  $\Delta\theta$  between a flat and cylindrical crystal caused by a rotation of the cylindrical axis  $\phi$  shown in Fig. 9(a) is given by:<sup>28</sup>

$$\Delta\theta = -\phi \frac{(1+M)\psi}{M\sin\theta} . \quad (13)$$

This angular error has the same linear  $\psi$  dependence as a uniform twist in the Bragg planes. For the X14 beamline, the bending rods were installed with  $|\phi| < 0.05^\circ$ . At  $M = 1$ , the conical geometry is half as sensitive to rotational errors  $\phi$  as the  $M = 0.33$  cylindrical geometry as shown by Eq. (13). In addition, the ability to adjust the twist of the curved crystal allows for a simple compensation of small angular errors from both twist and rotation misalignment. Small rotations of up to  $0.25^\circ$  (4 mrad) have a negligible effect upon transmission and rocking curve widths.

## 5.4 BENDING ERRORS

Once the two crystals have been aligned along the nominal beam axis, it is necessary to configure the second crystal to its desired conical form. A systematic method is followed while observing the radiation on a fluorescent screen. Consider the case where only one corner of the focusing crystal is pushed either too far or too little. The plate then undergoes a complicated distortion relative to the ideal conical shape. This distortion involves a twist of the plate, a change in radius from one side of the plate to the other, the wrong cone angle, and an error in the average curvature of the crystal. The complexity of the crystal distortion during single-motor motions makes it difficult to adjust the crystal bender one motor at a time. It is much more convenient to discuss the bending errors in terms of coupled motions involving all four motors as shown by the schematic images of the focus in Fig. 13. Four coupled errors are illustrated: average radius of crystal (focus), crystal twist (twist), cone error (cone), and uneven moment (even). These four errors can be separately corrected by observing the focal spot size, intensity, and uniformity and by observing changes in a partially focused image as the first crystal is scanned through the Bragg angle. These four linearly independent corrections can compensate for any distortion that can be corrected with individual motors.

### 5.4.1 Focus

First, the horizontal radiation swath intercepted by the crystal pair is semi-focused by moving all four rods motors as shown in Fig. 13(a-b). As the focused beam approaches 10- to 20-mm width, it is useful to scan the first flat crystal through  $\theta$  while observing the radiation pattern. In the semi-focused mode, the radiation pattern on the fluorescent screen should be uniform across its width and progressively become brighter, then fade out as  $\Delta\theta$  is scanned. If the radiation pattern is not uniform across the width of the image, then the curved crystal is not uniformly bent. An analysis of the nonuniformity of the radiation pattern and how it changes with  $\Delta\theta$  leads to the following set of corrections to be made to the shape of the curved crystal.

### 5.4.2 Twist

The first bending error to be corrected is a twist in the crystal. Twist results from a pattern of errors in the bending motor displacements as illustrated by the arrows or their reverse in Fig. 13(c). Crystal twist can be readily detected by observing the pattern of

partially focused radiation as the relative parallelism of the first and second crystals is adjusted by scanning the first crystal in  $\theta$ . The bright region of the transmitted beam is observed (fluorescent screen) to move from one side of the crystal to the other as  $\Delta\theta$  is varied. The twist error is removed by driving the four motors as illustrated by the arrows in Fig. 13(c).

ORNL-DWG 92-11018

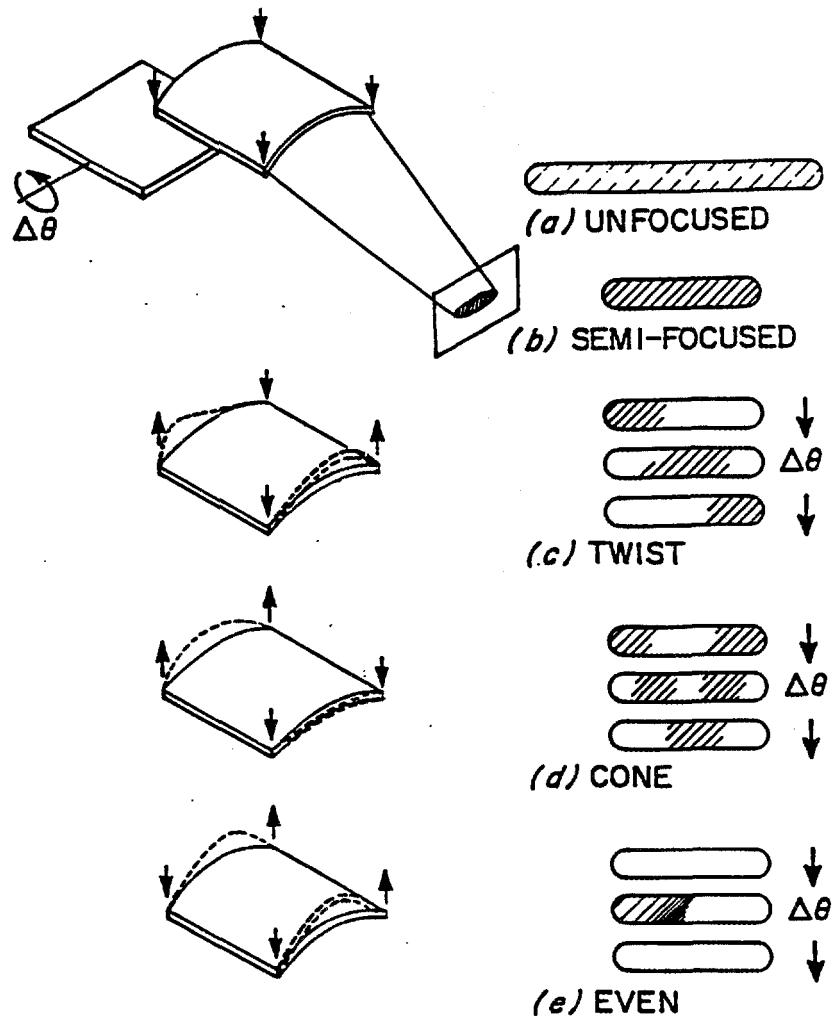


Fig. 13. (a-e) Schematic showing how four orthogonal bending motions are used to achieve a conical curvature for a four-line loaded plate. (a-b) If all four ends of the bender illustrated in Fig. 7 are driven equally, the average radius is changed. (c) If diagonally opposing motors are driven in the same direction, then the plate is twisted. (d) When front and back ends are driven, then the cone angle  $\Delta$  is changed. (e) Left-side motors driven in the opposite direction of right-side motors cause the radius to increase on one side of the crystal and decrease on the other side.

A pair of diagonally opposed motors is driven in the same direction and the other pair in the opposite direction until the diffracted radiation remains bilaterally symmetric on scanning  $\Delta\theta$ .

#### 5.4.3 Cone Angle

Errors in the cone angle of the crystal [Fig. 13(d)] are detected by again changing  $\Delta\theta$  and observing the transmitted pattern for a partially focused beam. Cone angle errors cause the bright part of the beam to move symmetrically inward or outward from the central ray with  $\Delta\theta$  depending on the sign of the cone error and the sign of the  $\Delta\theta$  scan. Motors are driven as illustrated by the arrows (or their reverse) in Fig. 13(d) to change the radius from front to back until the entire horizontal beam divergence is passed simultaneously.

#### 5.4.4 Even (Symmetric) Bending Moment

A third, but less common, error occurs when the bending moment across the crystal is not symmetric. This results in an image with an overfocused side and an underfocused side as illustrated in Fig. 13(e). This error is observed without adjusting  $\Delta\theta$  and is removed by driving the four motors as illustrated in Fig. 13(e). Iterations of these three adjustments are made to achieve a uniform intensity distribution for the semi-focused beam.

The final adjustment to achieve a minimum focal spot is to change the average curvature as discussed in Sect. 5.4.1. Curvature is adjusted by translating all four corners of the bender equally [Fig. 13(a-b)] until the smallest beam size is achieved. In general, several iterations of the adjustments described above are required during initial installation of a crystal. After the crystal has been aligned, the displacements required to reconfigure the crystal at a new energy can be easily calculated, and the crystal can be dynamically bent under computer control as energy is varied. We have found that only small manual adjustments are required to achieve best focus and efficiency for even, large energy shifts of 4 to 8 keV (0.6 to 1.3 fJ).

### 5.5 PERFORMANCE AND FUTURE APPLICATIONS

Some aspects of the performance of sagittal crystal monochromators have been reported.<sup>11,23,29-32</sup> We have shown that, at X14, the measured RMS focal spot size with a vertical focusing cylindrical mirror and a conical crystal, two-crystal monochromator is 0.36 mm

horizontal by 0.24 mm vertical.<sup>23</sup> This spot size is close to the theoretical focal spot size of 0.28 by 0.16 mm for no aberrations. The measured transmission is within 20% of the theoretical value.

Following our lead, others have successfully constructed similar bending devices and ribbed crystals.<sup>29-32</sup> The four-rod bending scheme allows adequate control for correction of both the conical angle and the crystal twist during dynamical bending. Measurements show that the angular mixing of the horizontal divergence into the vertical divergence is small as predicted by the equation shown in Fig. 2(c). For mirrors, the mixing is 25 times larger for the same sagittal divergence.

With the highly collimated radiation sources from undulators, it may be possible to constrain crystals with no ribs over the region that intercepts the X-ray beam. This would permit more ideal focusing to be achieved. For example, the anticipated RMS source size and divergences (horizontal and vertical) for an undulator on the APS are 0.31 by 0.085 mm<sup>2</sup> and 0.024 by 0.009 mrad<sup>2</sup>, respectively.<sup>22</sup> At 30 m, the RMS beam size will only be 0.78 by 0.11 mm so that a rib spacing with a 3-mm gap will collect 95% of the beam and avoid a rib over the beam intercept. This spacing is only slightly wider than the 2-mm gap successfully used with existing ribbed crystals. Simple cylindrical shapes are adequate for such small divergences. Sagittal focusing can also be used with inclined-high heat load crystals at magnification of one-sixth to two (ref. 33). Because of the large distances from the source, focusing optics for third-generation undulators are desirable as they can increase the intensity at the sample by factors of 20 or more.

## 6. CONCLUSION

The conical geometry discussed here can be used to focus radiation by either total external reflection or diffraction. The essential feature is that a conical geometry can intercept rays in a fan of X rays at an angle independent of sagittal divergence and can condense the fan. With dynamical bending, we have efficiently focused X rays from 3 to 30 keV (0.48 to 4.8 fJ). X rays from a first, flat Si<sub>111</sub> crystal were condensed by an Si<sub>111</sub> crystal bent with a simple four-rod bender. While a cylindrical geometry works well at  $M = 0.33$ , conical curvature allows efficient focusing from  $M \sim 0.2$  to 2. In addition, the conical geometry more nearly preserves the brightness of the source.

## 7. ACKNOWLEDGMENTS

We appreciate useful discussions with P. Eng and G. Rosenbaum concerning their implementation of sagittal crystal focusing and with E. D. Specht and J. L. Robertson for useful comments on the manuscript. We thank M. L. Hodges for final report preparation and K. Spence for editing. Research performed in part at NSLS, sponsored by the Division of Chemical Sciences, and at ORNL, sponsored by the Division of Materials Sciences, U.S. Department of Energy, under contract DE-AC05-84OR21400 with Martin Marietta Energy Systems, Inc.

## 8. REFERENCES

1. H. H. Johann, "Die Erzeugung Lichtstarker Rontgenspektren mit Hilfe von Konkavkristallen," *Z. Phys.* **69**, 185-206 (1931).
2. T. Johannson, "Uber ein neuartiges genau fokussierendes Rontgenspektrometer," *Z. Phys.* **82**, 507-28 (1933).
3. L. V. Von Hamos, "Rontgenspektroskopie und Abbildung mittels gekrummter Kristallreflektoren," *Annalen der Physik* **17**, 716-24 (1933); "Formation of true X-ray images by reflection on crystal mirrors," *Z. Kristal.* **101**, 17 (1939); and *Arik. Mat. Astr. Fys.* **31A**, 1 (1945).
4. H. Winick and S. Doniach, *Synchrotron Radiation Research*, Plenum Press, New York, 1980.
5. E. E. Koch, *Synchrotron Radiation Sources*, pp. 225-74 in *Interaction of Radiation with Condensed Matter Vol. II*, International Atomic Energy Agency, Vienna, Austria, 1977.
6. J. B. Hastings, B. M. Kincaid, and P. Eisenberger, "A separated function focusing monochromator system for synchrotron radiation," *Nucl. Instrum. Methods Phys. Res.* **152**, 167-71 (1978).
7. M. Lemonnier, R. Fourme, F. Rousseaux, and R. Kahn, "X-ray curved-crystal monochromator system at the storage ring DCI," *Nucl. Instrum. Methods Phys. Res.* **152**, 173-77 (1978).
8. J. Hendrix, M. H. J. Koch, and J. Bordas, "A double focusing X-ray camera for use with synchrotron radiation," *J. Appl. Cryst.* **12**, 467-77 (1979).

9. C. J. Sparks, Jr., S. Raman, E. Ricci, R. V. Gentry, and M. O. Krause, "Evidence against Superheavy Elements in Giant-Halo Inclusions Re-examined with Synchrotron Radiation", *Phys. Rev. Lett.* **40**, 507-11 (1978); G. E. Ice and C. J. Sparks, "Mosaic crystal X-ray spectrometer to resolve inelastic background from anomalous scattering experiments," *Nucl. Instrum. Methods Phys. Res., Sect. A* **A291**, 110-16 (1990).
10. C. J. Sparks, Jr., B. S. Borie, and J. B. Hastings, "X-ray monochromator for focusing synchrotron radiation above 10 keV," *Nucl. Instrum. Methods Phys. Res.* **172**, 237-42 (1980).
11. C. J. Sparks, G. E. Ice, J. Wong, and B. W. Batterman, "Sagittal focusing of synchrotron x-radiation with curved crystals," *Nucl. Instrum. Methods Phys. Res.* **194**, 73-78 (1982).
12. B. W. Batterman and L. Berman, "Sagittal focusing of synchrotron radiation," *Nucl. Instrum. Methods Phys. Res.* **208**, 327-31 (1983).
13. G. E. Ice and C. J. Sparks, "Diffraction crystals for sagittally focusing x-rays," U.S. Patent 4,461,018, July 17, 1984.
14. J. A. Howell and P. Horowitz, "Ellipsoidal and bent cylindrical condensing mirrors for synchrotron radiation," *Nucl. Instrum. Methods Phys. Res.* **125**, 225-30 (1975).
15. S. Aoki and Y. Sakayanagi, "X-ray imaging with toroidal mirrors," *Jpn. J. Appl. Phys.* **17-2**, 457-60 (1978).
16. S. M. Heald, "Application of bent cylindrical mirrors to X-ray beam lines," *Nucl. Instrum. Methods Phys. Res.* **195**, 59-62 (1982).
17. U. Kaminaga, T. Matsushita, and K. Kohra, "Curvature Dependence of Reflection Profiles of Silicon Curved Crystal Monochromators as Measured with Double-Crystal (n,n) Setting," *Jpn. J. Appl. Phys.* **17-2**, 453-56 (1978).
18. B. E. Warren, *X-Ray Diffraction*, Chapter 14, Dover Publications, Inc., New York, 1969.
19. J. A. Golovchenko, R. A. Levesque, and P. L. Cowan, "An X-ray Monochromator System for Use With Synchrotron Radiation Sources," *Rev. Sci. Instrum.* **52**, 509 (1981).
20. A. Franks, "X-ray Optics," *Sci. Prog. Oxford* **64**, 371-422 (1977).
21. P. Kirkpatrick and A. V. Baez, "Formation of Optical Images by X-rays," *J. Opt. Soc. Am.* **38**, 766-74 (1948).

22. G. K. Shenoy, P. J. Viccaro, and D. M. Mills, "Characteristics of the 7-GeV Advanced Photon Source: A Guide for Users," ANL-88-9, Argonne National Laboratory, Argonne, Ill., 1988.
23. A. Habenschuss, G. E. Ice, C. J. Sparks, and R. A. Neiser, "The ORNL beamline at the National Synchrotron Light Source," *Nucl. Instrum. Methods Phys. Res., Sect. A* **A266**, 215-19 (1988).
24. J. P. Den Hartog, *Strength of Materials*, Chapter III, Dover Publications, New York, 1949.
25. M. S. Troitsky, *Stiffened Plates, Bending, Stability and Vibration*, Elsevier, New York, 1976.
26. See, for example, R. P. Feynman, R. B. Leighton, and M. Sands, p. 38-11 in *The Feynman Lectures on Physics*, Addison Wesley, Reading, Mass., 1963.
27. H. Kawata, M. Sato, T. Iwazumi, M. Ando, N. Sakai, M. Ito, Y. Tanaka, N. Shiotani, F. Itoh, H. Sakurai, Y. Sakurai, Y. Watanabe, and S. Nanao, "Water-cooled quasi-doubly bent crystal monochromator for Compton scattering experiments," *Rev. Sci. Instrum.* **62**, 2109 (1991).
28. A. Koyama, M. Nomura, H. Kawata, T. Iwazumi, M. Sato, and T. Matsushita, "Improvement of a sagittally focusing double-crystal monochromator," *Rev. Sci. Instrum.* **63**, 916-19 (1992).
29. M. Bessiere, R. Kahn, G. Gravant, A. Lena, E. Elkaim, S. Lefebvre, and R. Bosshard, "Sagittal focusing on line D23," *Lure BIS Annual Report*, 1989; and E. Elkaim, S. Lefebvre, R. Kahn, J. F. Berar, M. Lemonnier, and M. Bessiere, "Diffraction and diffuse scattering measurements in material science: Improvement brought to a six-circle goniometer on a synchrotron beam line," *Rev. Sci. Instrum.* **63**, 988-91 (1992).
30. P. Eng, "High Resolution Surface X-Ray Diffraction Study of Pb Monolayer Superlattice Ordering Kinetics on Ni (001)," unpublished Ph.D. dissertation, State University of New York at Stony Brook, 1991; and P. W. Stephens, P. J. Eng, and T. Tse, "Construction and performance of a bent crystal X-ray monochromator," *Rev. Sci. Instrum.* **64**, 374 (1993).
31. G. M. Lamble and S. M. Heald, "Operation of a dynamically bent sagittally focusing double crystal monochromator for XAFS studies," *Rev. Sci. Instrum.* **63**, 880-84 (1992).
32. G. Rosenbaum, M. Sullivan, R. Fischetti, and L. Rock, "Sagittally focusing scanning monochromator produces 0.4-mm focus," *Rev. Sci. Instrum.* **63**, 931 (1992).
33. G. E. Ice and C. J. Sparks, "Sagittal crystal focusing of undulator radiation with high heat load inclined crystals," *SPIE 1740* **11**, (1992).



**INTERNAL DISTRIBUTION**

- |                                    |                                  |
|------------------------------------|----------------------------------|
| 1-2. Central Research Library      | 19. E. A. Kenik                  |
| 3. Document Reference Section      | 20-70. C. J. Sparks              |
| 4-5. Laboratory Records Department | 71. E. D. Specht                 |
| 6. Laboratory Records, ORNL RC     | 72. Y. A. Chang (Consultant)     |
| 7. ORNL Patent Section             | 73. H. W. Foglesong (Consultant) |
| 8-10. M&C Records Office           | 74. J. J. Hren (Consultant)      |
| 11. B. R. Appleton                 | 75. M. L. Savitz (Consultant)    |
| 12. L. L. Horton                   | 76. J. G. Simon (Consultant)     |
| 13. C. R. Hubbard                  | 77. K. E. Spear (Consultant)     |
| 14-18. G. E. Ice                   |                                  |

**EXTERNAL DISTRIBUTION**

78. ALLIED-SIGNAL, INC., Department of Engineered Products, 50 East Algonquin Road, DesPlaines, IL 60017-5016

H. J. Robota

- 79-91. ARGONNE NATIONAL LABORATORY, 9700 South Cass Avenue, Argonne, IL 60439

P. L. Cowan (Physics Division, Bldg. 203)  
 A. M. Khounsary (Experimental Facilities Division/APS, Bldg. 362)  
 G. Knapp (Materials Science Division, Bldg. 223)  
 V. I. Kushnir (Experimental Facilities Division/APS, Bldg. 362)  
 A. T. Macrander (Experimental Facilities Division/APS, Bldg. 362)  
 V. A. Maroni (Chemical Technology Division, Bldg. 205)  
 D. Mills (Experimental Facilities Division/APS, Bldg. 362)  
 D. E. Moncton (Office of the Director/APS, Bldg. 360)  
 P. A. Montano (Materials Science Division, Bldg. 223)  
 M. Ramanathan (Materials Science Division, Bldg. 223)  
 G. Shenoy (Experimental Facilities Division/APS, Bldg. 362)  
 E. M. Westbrook (Biological and Medical Research Division, Bldg. 202)  
 W. Yun (Experimental Facilities Division/APS, Bldg. 362)

92. AT&T BELL LABORATORIES, Department 11121, 600 Mountain Avenue, Rm. 1G-362, Murray Hill, NJ 07974

M. A. Marcus

93. AT&T BELL LABORATORIES, 600 Mountain Avenue, Rm. IE334, Murray Hill, NJ 07928

R. M. Fleming

- 94-102. BROOKHAVEN NATIONAL LABORATORY, Upton, NY 11973

L. Berman (725D NSLS)  
 A. Bommanavar (X18B 725A NSLS)  
 D. Chapman (725D NSLS)  
 P. Eng (X16A 725A)  
 J. Hastings (725D NSLS)  
 S. M. Heald (Dept. DAS, Bldg. 480)  
 E. Isaacs (X16B, 725A, NSLS)  
 M. Rivers (Bldg. 815)  
 G. Rosenbaum (X9 725A NSLS)

- 103-104. CORNELL UNIVERSITY, Ithaca, NY 14853

B. Batterman (Cornell High Energy Synchrotron Source, 210A Clark Hall)  
 D. Bilderback (281 Wilson Laboratory)

- 105-107. EUROPEAN SYNCHROTRON RADIATION FACILITY, Bldg. 2, B.P. 220, F-38043, Grenoble Cedex, France

A. Freund (Rm. 255)  
 A. Kvik (Rm. 262)  
 P. Suortti (Rm. 255)

108. EXXON RESEARCH & ENGINEERING COMPANY, c/o Brookhaven National Laboratory, Exxon P.R.T., Building 510E, Upton, NY 11973

R. Hewitt

109. EXXON RESEARCH & ENGINEERING COMPANY, CR Department, Route 22 East, Annandale, NJ 08801

S. K. Sinha

110. GEORGIA INSTITUTE OF TECHNOLOGY, School of Materials Engineering, Atlanta, GA 30332-0245

S. R. Stock

111. HAMBURGER SYNCHROTRON STRAHLUNGLABOR, HASYLAB at DESY,  
Notkestrasse 85, D-2000, Hamburger 52, Germany  
G. Materlick
112. HOWARD UNIVERSITY, Department of Physics & Astronomy, 2355 6th Street,  
Rm. 105, Washington, DC 20059  
W. P. Lowe
113. ILLINOIS INSTITUTE OF TECHNOLOGY, Department of Physics, 3301 South  
Dearborn Street, Chicago, IL 60616  
T. I. Morrison
- 114-115. IOWA STATE UNIVERSITY, Department of Physics, Ames Laboratory, Ames,  
IA 50011  
A. I. Goldman  
D. W. Lynch
116. LAWRENCE LIVERMORE NATIONAL LABORATORY, P. O. Box 808, L-278,  
Livermore, CA 94550  
K. Skulina
117. NORTHWESTERN UNIVERSITY, Department of Physics & Astronomy,  
2145 Sheridan Road, Evanston, IL 60208-3112  
P. Dutta
118. NORTHWESTERN UNIVERSITY, Dow, Northwestern Diffraction CAT Synchrotron  
Research Center, 1033 University Place, Ste. 140, Evanston, IL 60201  
J. P. Georgopoulos
119. PURDUE UNIVERSITY, Department of Physics, West Lafayette, IN 47907  
R. Colella
- 120-121. STANFORD LINEAR ACCELERATOR CENTER, P. O. Box 4349, Mail Stop 69,  
Stanford, CA 94309  
P. Pianetta  
H. Winick

- 122-123. THE UNIVERSITY OF CHICAGO, Consortium for Advanced Radiation Source,  
5640 South Ellis Avenue, Chicago, IL 60637

W. Schildkamp  
P. J. Viccaro

124. UNIVERSITY OF CALIFORNIA-SANTA CRUZ, Department of Physics,  
Santa Cruz, CA 94307

G. S. Brown

125. UNIVERSITY OF ILLINOIS, c/o Brookhaven National Laboratory, Materials  
Research Laboratory, Bldg 725, NSLS X-14, Upton, NY 11973

M. C. Nelson

- 126-127. UNIVERSITY OF ILLINOIS, Materials Research Laboratory, 104 South Goodwin,  
Urbana, IL 61801

H. K. Birnbaum  
H. Hong

128. UNIVERSITY OF ILLINOIS, Department of Materials Science and Engineering,  
1304 Green Street, Urbana, IL 61801

H. Chen

129. UNIVERSITY OF NOTRE DAME, Department of Physics, Notre Dame, IN 46556

B. A. Bunker

130. UNIVERSITY OF WASHINGTON, Department of Physics, FM-15, Seattle,  
WA 98195

E. A. Stern

131. UNION IL PRODUCTS RESEARCH CENTER, 50 East Algonquin Road,  
DesPlaines, Il 60017

R. W. Broach

132. X-RAY ANALYTICS, P. O. Box 678, Upton, NY 11973

K. L. D'Amico

133. DEPARTMENT OF ENERGY, Office of Basic Energy Sciences, ER-132,  
Washington, DC 90545

W. Oosterhuis

135-136. U.S. DOE, OAK RIDGE OPERATIONS OFFICE, P.O. Box 2008, Oak Ridge,  
TN 37831

Deputy Assistant Manager for Energy Research and Development  
E. E. Hoffman

137-138. U.S. DOE, OFFICE OF SCIENTIFIC AND TECHNICAL INFORMATION,  
P.O. Box 62, Oak Ridge, TN 37831

For distribution by microfiche as shown in DOE/OSTI-4500,  
Distribution Category UC-25 (Materials)